

1 Late Permian–Middle Triassic magnetostratigraphy in North China and its  
2 implications for terrestrial-marine correlations

3 Wenwei Guo<sup>a</sup>, Jinnan Tong<sup>a</sup> \*, Qi He<sup>b</sup>, Mark W. Hounslow<sup>c, d</sup>, Huyue Song<sup>a</sup>, Jacopo Dal  
4 Corso<sup>a</sup>, Paul B. Wignall<sup>e</sup>, Jahandar Ramezani<sup>f</sup>, Li Tian<sup>a</sup>, Daoliang Chu<sup>a</sup>

5 <sup>a</sup>*State Key Laboratory of Biogeology and Environmental Geology, School of Earth Science, China*  
6 *University of Geosciences, Wuhan 430074, China*

7 <sup>b</sup>*State Key Laboratory of Geological Processes and Mineral Resources, Planetary Science Institute,*  
8 *School of Earth Sciences, China University of Geosciences, Wuhan 430074, China*

9 <sup>c</sup>*Lancaster Environment Centre, Lancaster University, Lancaster, UK*

10 <sup>d</sup>*Earth, Ocean and Ecological Sciences, University of Liverpool, Liverpool, Jane Herdman Building,*  
11 *UK*

12 <sup>e</sup>*School of Earth and Environment, University of Leeds, Leeds, UK*

13 <sup>f</sup>*Department of Earth, Atmospheric and Planetary Sciences, Massachusetts Institute of Technology,*  
14 *Cambridge, MA 02139, USA*

15 \*Corresponding author: jntong@cug.edu.cn (J.N. Tong)

16

17 **Abstract**

18 A detailed magnetostratigraphic study, tied to a new latest Permian U–Pb ID-TIMS radioisotopic  
19 age from an ash bed, was carried out from the continental Shichuanhe section in North China in  
20 order to provide a magnetic polarity scale from the Late Permian–early Middle Triassic. The tilt-  
21 corrected mean directions of the characteristic remanent magnetization pass the reversal test and  
22 correspond to a site paleolatitude of 18.1°N during the Early Triassic, consistent with previous

23 results from the North China Block. The magnetostratigraphy shows excellent similarity with  
24 previous studies, allowing interregional correlations to other marine and non-marine records.  
25 Normal magnetozones SCH3n, constrained by an absolute age of  $252.21 \pm 0.15$  Ma from 3.5 m below  
26 its base, is unambiguously correlated to the earliest Triassic normal magnetochron LT1n. This newly  
27 established magnetostratigraphic framework and published carbon-isotope chemostratigraphy  
28 indicate the Permian–Triassic Boundary (PTB) is ca. 8 m above the base of SCH3n (within the  
29 middle part of the Sunjiagou Formation) and additionally demonstrates a continuous PTB sequence  
30 at SCH. The overlying reverse polarity dominated interval (SCH3r–SCH5r) to the middle Liujiagou  
31 Formation, straddles an interval from the mid-Griesbachian to mid-Smithian. The base of the  
32 Olenekian is provisionally located in the lower part of the Liujiagou Formation, near the base of  
33 magnetozones SCH5n. The succeeding thick normal magnetozones SCH6n persist into the upper  
34 Heshanggou Formation, with the inferred Smithian–Spathian boundary in the upper part of the  
35 Liujiagou Formation. The transition from reverse magnetozones SCH6r to the overlying normal  
36 magnetozones SCH7n, coincides with a clear erosional contact with the base of the Emaying  
37 Formation. Consequently, magnetozones SCH7n is matched to the Early Anisian magnetochron  
38 MT3n, with the Olenekian–Anisian boundary interval missing. Our new integrative timescale also  
39 provides additional magnetostratigraphic constraints on the terrestrial ecological crisis in North  
40 China, which lies within reverse magnetozones SCH2r, some  $270 \pm 150$  kyrs before the main marine  
41 extinction, that falls in the overlying normal magnetochron LT1n, as confirmed by the radioisotopic  
42 date.

43

44 **Key words:** Magnetostratigraphy, marine-terrestrial correlation, ID-TIMS age, terrestrial extinction

45

## 46 **1. Introduction**

47 The Late Permian–Middle Triassic is a key interval in the history of life, which is marked by the  
48 most severe extinction of the Phanerozoic, i.e., the Permian–Triassic mass extinction (PTME) at  
49 about 252 Ma (Wignall, 2015; Benton, 2018). Persistent environmental perturbations followed  
50 throughout the Early Triassic (Payne et al., 2004; Song et al., 2012; Sun et al., 2012; Wu et al.,  
51 2021b), resulting in a protracted biotic recovery for more than 5 Ma after the PTME (Chen and  
52 Benton, 2012), although marine ecosystem recovery was still underway in the latest Triassic (Song  
53 et al., 2018). Notably, knowledge about the timing, magnitude and duration of the PTME and its  
54 aftermath are largely derived from marine records because they are stratigraphically most complete,  
55 can be more easily correlated using biostratigraphy and are better constrained by absolute ages  
56 (Chen and Benton, 2012; Burgess et al., 2014).

57 In contrast, a full understanding of the PTME and its following biotic restoration on land is  
58 more challenging, due to the more varied depositional environments, probably less-continuous  
59 sedimentary record, and typically rather poorly age constrained. Recently, increasing studies have  
60 shed light on the timing of the terrestrial ecological crisis, which have argued for extinction on land  
61 preceding that in the oceans by about 50 kyr to 240–640 kyr, with differing paces among continental  
62 basins (Fielding et al., 2019, 2021; Chu et al., 2020; Gastaldo et al., 2020). Although knowledge  
63 about the PTME in terrestrial facies have improved, the relative timing of biological recovery on  
64 land cannot be easily compiled because a globally unified fine-scale chronostratigraphy is not  
65 available. Causal links between unusual sedimentary structures, such as microbial mats and possible  
66 hurricanes, during the Early Triassic linked to abnormal environmental conditions are also

67 challenging to understand (Chu et al., 2015, 2017; Ji et al., 2021). Therefore, a more integrative  
68 approach that allows events to be temporally constrained throughout the Early Triassic, using tool  
69 such as magnetostratigraphy, is required for a better appreciation of the global ecological evolution.

70 The global and synchronous nature of geomagnetic polarity boundaries has made  
71 magnetostratigraphy an important approach for precise correlation between successions, a tool  
72 which is independent of facies control. In the last two decades, significant progress has been  
73 achieved in establishing a comprehensive time-calibrated magnetostratigraphy during the Permian  
74 and Triassic, that provides a scale for interregional correlations (e.g., Steiner, 2006; Hounslow and  
75 Muttoni, 2010; Hounslow and Balabanov, 2018). Reliable PTB magnetostratigraphies have also  
76 been constructed in continental successions, including in Europe and eastern Australia (Szurlies,  
77 2003; Szurlies et al., 2013; Belica, 2017), but a detailed continental-succession based magnetic  
78 stratigraphy through the entire Early Triassic is only available in the Central European Basin  
79 (Szurlies, 2007). However, magnetostratigraphy in North China, straddling the complete Late  
80 Permian to Middle Triassic has been rarely undertaken and a detailed regional polarity reversal  
81 pattern is difficult to unravel owing to the coarse spatial sampling and lack of specific correlation  
82 anchors (e.g., using biostratigraphy, radioisotopic ages). Thus, regional lithostratigraphic templates  
83 have been widely used (Ma et al., 1992; Embleton et al., 1993).

84 We present a high resolution magnetostratigraphy from the Upper Permian throughout the  
85 Lower Triassic to the earliest Anisian (Middle Triassic) in central North China. A new U-Pb CA-  
86 ID-TIMS (chemical abrasion isotope dilution thermal ionization mass spectrometry) age from an  
87 ash bed within the middle part of the Sunjiagou Formation provides a geochronological anchor for  
88 the new magnetostratigraphic framework. Coupled to available biostratigraphy and carbon-isotope

89 chemostratigraphy, our multi-disciplinary approach enables establishment of a detailed timescale  
90 on land from Late Permian–earliest Middle Triassic in North China, which locates the PTB at the  
91 Shichuanhe (SCH) section, and so understand the relative timing between the terrestrial PTME and  
92 marine extinctions.

93

## 94 **2. Geological setting**

95 The Ordos Basin was a large depocenter that formed part of the intracratonic central North China  
96 Basin, located at 10–20°N paleolatitude during the Paleozoic–Mesozoic transition, which was  
97 bordered by the Liupan-Helan-Yin-Lvliang uplands to the west and southeast and passed into further  
98 terrestrial basins to the northeast (Huang et al., 2018; Meng et al., 2019; Fig. 1A). Since  
99 cratonization, the Early Cambrian deposits in the North China Block were followed by a major  
100 hiatus in the Middle Ordovician to the Mississippian due to regional uplift. Sedimentation resumed  
101 after a major transgression in the Pennsylvanian, represented by alternating marine and terrestrial  
102 sequences with well-developed coals (Yang et al., 2017). During the Permian the North China block  
103 was largely comprised of terrestrial systems, in which coal forming environments ceased in the  
104 upper Shihhotse Formation in the Early Permian, according to ID-TIMS dating (Wu et al., 2021a).  
105 The Permian–Triassic Shiqianfeng Group is characterized by red beds, which contains rare body  
106 fossils that are inadequate to establish a detailed biostratigraphy (Tong et al., 2019). This interval is  
107 also poorly dated apart from two LA-ICP-MS ages obtained from detrital zircons (Zhu et al., 2019;  
108 Fig. 1C). However, a mixed terrestrial spinicaudatan-marine bivalve assemblage, a consequence of  
109 a regional marine transgression in the southern Ordos Basin, allows identification of the Permian–  
110 Triassic transitional beds at SCH (Chu et al., 2019).

111 The Shiqianfeng Group is divided from base to top into the Sunjiagou, Liujiagou and  
112 Heshanggou formations, which are overlain by the Ermaying Formation (Fig. 1C). The Sunjiagou  
113 Formation consists of green sandstone with interbedded mudstone in the lower part, containing a  
114 Late Permian *Ullmannia bronniei-Pseudovoltzia cf. libeana* flora assemblage (Lu et al., 2020),  
115 representing deposition in fluvial channels and point bars (Zhu et al., 2019, 2020). However, this  
116 unit is not well exposed at SCH and thus, the nature of the boundary with the underlying strata is  
117 unclear. The overlying portion is characterized by a color change to a sequence of dominantly red  
118 siltstones, with well-developed paleosols that formed on a floodplain (Zhu et al., 2020). This is  
119 followed by alternating thin, fine-grained sandstones, massive mudstones and marlstones, with rare  
120 ripple marks, and desiccation cracks, interpreted as the deposits of a coastal facies with occasional  
121 drying (Yu et al., 2022; Ji et al., under review). The time interval covered by the Sunjiagou  
122 Formation is controversial, with the supposed PTB, defined by tetrapods, organic carbon isotopes  
123 and mixed marine-terrestrial biota, having a position postulated to range from the mid to the top of  
124 the Sunjiagou Formation (Chu et al., 2019; Zhu et al., 2019, 2020; Lu et al., 2020; Wu et al., 2020).

125 The mud-rich floodplain and coastal facies of the Sunjiagou Formation were interrupted by a  
126 pronounced change to the fluvial-dominated, sandstone-rich Liujiagou Formation (Zhu et al., 2020;  
127 Ji et al., 2021). Conglomeratic intraclasts, concentrically-laminated concretions and microbial mats  
128 are found within the interlayered lacustrine facies of the Liujiagou Formation (Chu et al., 2015,  
129 2017; Ji et al., 2021). Aeolian deposits are also reported from the northern part of the basin (Zhu et  
130 al., 2020). The Liujiagou Formation contains very rare fossils, with plants attributed to the  
131 *Pleuromeia jiaochengensis* assemblage in the middle to upper parts (Wang and Wang, 1990). The  
132 base of the Liujiagou Formation has traditionally been considered conformable, although a

133 disconformity has also been suggested (IGCAGS, 1980).

134 The overlying Heshanggou Formation is marked by a return to dominantly dark red mudstones  
135 and siltstones, which rest conformably on the underlying strata. Laterally persistent sandstones  
136 become dominant upwards, and primary sedimentary structures are hard to detect due to well-  
137 developed paleosols and bioturbation throughout the formation (Guo et al., 2019; Yu et al., 2022).  
138 The fluvial overbank and shallow lacustrine facies interpreted for the Heshanggou Formation (Zhu  
139 et al., 2020) contain diverse fossils (e.g., vertebrates, ostracods and sporomorphs), which are  
140 indicative of the late Early Triassic (IGCAGS, 1980).

141 The succeeding Ermaying Formation is characterized by massive green fluvial sandstones with  
142 interbedded green and red mudstones and conglomerates, which probably rest conformably on the  
143 underlying strata (IGCAGS, 1980). However, the basal sandstones of the Ermaying Formation at  
144 SCH contain imbricated conglomerates and large mud clasts, implying a basal erosional contact,  
145 suggestive of a possible local hiatus (Supplementary Fig. S1). The *Parakannemeyeria* fauna and an  
146 Anisian U-Pb ID-TIMS age of  $243.528 \pm 0.069$  Ma suggest the Ermaying Formation is Middle  
147 Triassic in age (Liu et al., 2018).

148

### 149 **3. Materials and methods**

#### 150 **3.1 Paleomagnetic methods and analysis**

151 Magnetostratigraphic, sedimentological and geochronological analyses were undertaken at the  
152 Shichuanhe section (GPS: 35.03°N, 108.88°E), located near Tongchuan, 90 km north of Xi'an City,  
153 Shaanxi Province. Magnetostratigraphic samples were collected throughout the section, using both  
154 hand samples, oriented in situ by a magnetic compass, and oriented core-plugs made by a portable

155 field drill. In total, 272 hand samples from fine-grained sediments and marlstones, and 39 core plugs  
156 from sandstones, were collected, covering an interval spanning the inferred Late Permian to basal  
157 Middle Triassic (Supplementary Fig. S2). Sample spacing ranges from 0.5 to 2.5 m, depending on  
158 suitable lithologies. In the laboratory, 56 hand samples were excluded from paleomagnetic studies  
159 because they were too fractured and could not be prepared into specimens. Each of the remaining  
160 samples was cut into at least two 2 cm cubes or 2 cm long cylinders for paleomagnetic measurements.

161 All specimens were subjected to stepwise thermal demagnetization using 16–19 steps (up to  
162 680°C) in a Magnetic Measurements ASC TD48 thermal specimen demagnetizer. Each heating was  
163 followed by cooling in a residual magnetic field  $\leq 20$  nT. Specimens were housed in a magnetically  
164 shield room with ambient magnetic field  $\leq 300$  nT and measured on a 2G Enterprises 755-4K U-  
165 Channel magnetometer at the China University of Geosciences (Wuhan), China. Characteristic  
166 remanent magnetization directions (ChRMs) were isolated using principal component analysis, as  
167 implemented in the PuffinPlot software (Lurcock and Wilson, 2012). Both linear trajectory fits and  
168 great circles (remagnetization circles) were used in defining the paleomagnetic behaviors. The  
169 PMAGTOOL v5. software (Hounslow, 2006) was also used for calculation of mean directions,  
170 virtual geomagnetic poles (VGP) and performing the reversal tests. The ChRM directions isolated  
171 were classified into different categories based on their demagnetization behavior and quality, similar  
172 to the method of Hounslow et al. (2008). ChRMs displaying clear linearity or exhibiting great-circle  
173 trends were categorized into S-type or T-type behaviors, respectively. For S-type data, specimens  
174 were subdivided into three quality levels (S1, S2 and S3) based on the visual noisiness and length  
175 of colinear points, with S1 showing best quality and S3 the lowest quality. T-type data were also  
176 reclassified into three levels (T1, T2 and T3) according to the visual length and scatter of the



177 demagnetization points about the great circle, with T1 having the best-quality great circle trend,  
178 which terminated near the expected Triassic direction, and T3 for the poorer results. Specimen  
179 demagnetization results were interpreted with a polarity quality rating on the basis of a semi-  
180 subjective judgment (e.g., for normal polarity, N=best quality, N?=intermediate quality and N??  
181 =poorest quality). Specimens without an interpreted Permian–Triassic magnetizations are labelled  
182 as X quality. Poorer quality data (e.g., S3 and T3 demagnetization behaviors) were not used for  
183 mean direction calculations, but were used for VGP latitude calculations.

184       Representative specimens from green and red lithologies were selected to determine the main  
185 magnetic remanence carriers using magnetic susceptibility versus temperature experiments (K-T  
186 curves). Specimens were heated up to 700°C in air at 10°C/min, and subsequently cooled at the  
187 same rate to room temperature. The K-T curves were measured using an AGICO, MFK1-FA  
188 Kappabridge, at the China University of Geosciences (Wuhan).

189

### 190 **3.2 U-Pb geochronology**

191 Zircons were separated from a ~1 cm thick ash bed in the middle part of the Sunjiagou Formation  
192 at SCH. Forty extracted zircons were subjected to U-Pb LA-ICP-MS (Laser Ablation Inductively  
193 Coupled Plasma Mass Spectrometry) at the Mineral Rock Laboratory, Hubei Province Geological  
194 Experimental Testing Center, before being analyzed by the U-Pb CA-ID-TIMS method at the  
195 Massachusetts Institute of Technology (MIT) Isotope Laboratory, USA. General analytical  
196 procedures of the ID-TIMS experiment are described in [Ramezani et al. \(2011\)](#). Detailed U-Pb  
197 methods are provided in Supplementary Data A. Seven chemically abraded zircons were spiked with  
198 the EARTHTIME ET535 mixed U-Pb tracer before complete dissolution in HF, purification of Pb

199 and U by column chemistry and measurement of the Pb and U isotopes on the mass spectrometer.

200 Complete LA-ICP-MS results and U-Pb isotopic data are given in Supplementary Data C. The  
201 weighted mean age uncertainty of ID-TIMS is reported at 95% confidence interval and in the format  
202  $\pm x/y/z$  Ma, where x is the analytical (internal) uncertainty only, y includes the additional tracer  
203 calibration error and z includes the latter as well as the  $^{238}\text{U}$  decay constant error of [Jaffey et al.](#)  
204 [\(1971\)](#).

205

## 206 **4. Results**

### 207 **4.1 Rock magnetism**

208 Susceptibility of most of the red specimens consistently reduces at around 700°C, which is attributed  
209 to hematite. One sample exhibits a large rise in susceptibility at 450°C (from thermal alteration), but  
210 subsequently decreases at 585°C and 680°C, suggesting the presence of both magnetite and hematite.  
211 The susceptibility of green lithologies generally show curve inflexions at around 585°C,  
212 corresponding to the Curie temperature of magnetite. Therefore, magnetite and hematite appear to  
213 be the main magnetic remanence carriers of the magnetization in green and red sediments,  
214 respectively (Supplementary [Fig. S4](#)). A decline in susceptibility below 100°C in many samples may  
215 be due to goethite. The magnetization carriers are consistent with the thermal demagnetization  
216 behavior of the natural remanent magnetization (NRM) and previous investigations ([Yang et al.](#),  
217 [1991](#)).

218

### 219 **4.2 U-Pb geochronology**

220 Fifteen grains from forty zircons analyzed by LA-ICP-MS, with a high concordance, yield ages of

221 263±2.7 Ma to 249±2.5 Ma, and nine grains display ages that cover the PTB (Supplementary Fig.  
222 S5 and Supplementary data C). Five chemically abraded single zircon grains yielded overlapping  
223 <sup>206</sup>Pb/<sup>238</sup>U dates, with a weighted mean of 252.21±0.15 Ma and a mean square of weighted  
224 deviates (MSWD) of 0.45 (Fig. 5). But one analysis produced a significantly younger Jurassic age,  
225 which are in conflict with regional sediment sources and LA-ICP-MS results, and thus was rejected  
226 (See Supplementary Data A for discussion). The weighted mean date is the best estimate for the  
227 (maximum) age of deposition of the corresponding ash bed.

228

### 229 4.3 Paleomagnetic properties

230 Commonly, the untreated NRM intensities range between 0.1–10 mA/m, with a few exceptions up  
231 to 30 mA/m (Fig. 4 and Supplementary Fig. S3). There was considerable variation in  
232 demagnetization behavior between different lithologies. But usually, specimens showed two  
233 components, a low-temperature component (LTC) and a high-temperature component (HTC), which  
234 could be isolated during thermal demagnetization. More details about the demagnetization behavior  
235 and polarity interpretations are in Supplementary files A and B.

236 (a) A LTC was obtained in most specimens, which generally unblocked between NRM to ca.  
237 200–450°C (Fig. 2B–2E, 2H–2I). This LTC is generally northerly directed with a relatively steep  
238 inclination in geographic coordinates (Fisher mean of D=355.4°, I=55.3°,  $\alpha_{95}$ =5.1°, n=244; Fig.  
239 3A). The direction is comparable to the present-day field at the site (D=355.9°, I=54.1°, World  
240 Magnetic Model 2019–2024), which is inferred to be a recently acquired or more likely a Brunhes-  
241 age overprint.

242 (b) The HTC is isolated by both line fit and great circle fit (Fig. 2). Red and sometimes green

243 colored sediments fully demagnetized at 600–680°C, indicating hematite is the main carrier of the  
244 NRM (Fig. 2A–2E). A third of the greenish specimens became directionally erratic above 600°C,  
245 suggesting hematite is less important in these specimens (Fig. 2H). Some 55% of specimens display  
246 stable endpoints with a linear segment towards the origin in orthogonal projections (i.e., S-type; Fig.  
247 2A–2F), and 87% of line-fit results yield acceptable quality (S1 and S2) that could be used in a mean  
248 direction calculation (see Supplementary Table S1 for details). After tilt correction the mean normal-  
249 polarity HTC direction is concentrated in the NW with shallow positive inclination ( $D=325.0^\circ$ ,  
250  $I=34.0^\circ$ ,  $\alpha_{95}=2.9^\circ$ ,  $n=93$ ), and the mean reverse-polarity HTC direction is  $D=146.4^\circ$ ,  $I=-28.5^\circ$ ,  
251 ( $\alpha_{95}=4.9^\circ$ ,  $n=31$ ; Fig. 3B). The site paleolatitude of all the data converted to normal polarity is  
252  $17.7^\circ\text{N}$ , regardless of potential inclination shallowing produced during later compaction (Table 1).  
253 Paleomagnetic mean directions pass the reversal test with class Rb (McFadden and McElhinny,  
254 1990). A fold test is not possible due to the shallow bedding dips in the section.

255 (c) For the HTC, 37% of samples yield a great circle trend toward the characteristic directions.  
256 These were used for great circle fits to determine the unresolved directions (T-type; Fig. 2G–2I).  
257 About three-quarters of the T-type data display scatter terminating at around the observed mean S-  
258 class direction. T1 and T2 quality great circles were used in the mean direction calculation. A  
259 combination of line-fit ChRM directions and great circle poles (Fig. 3C), using the method of  
260 McFadden and McElhinny (1988), gave a combined mean direction for the HTC of  $D=325.6^\circ$ ,  
261  $I=33.3^\circ$  ( $\alpha_{95}=1.9^\circ$ ,  $n=197$ ), corresponding to a paleopole at  $55.2^\circ\text{N}$ ,  $359.0^\circ\text{E}$  ( $dp/dm=1.23/2.16$ ) and  
262 site paleolatitude of  $18.1^\circ\text{N}$  (Table 1). The combined mean directions have a positive reversal test  
263 with class Ra (McFadden and McElhinny, 1990).

264 The antipodal nature of the normal- and reverse-polarity subsets (Fig. 3B) and the statistically

265 similar directions compared to previously published Lower Triassic direction in nearby regions  
266 (Yang et al., 1991; Ma et al., 1992; Table 1), suggests that the magnetization is primary and obtained  
267 near the time of deposition.

268

#### 269 **4.4 Magnetostratigraphy**

270 The line-fit ChRM directions were converted to virtual geomagnetic pole (VGP) latitude using the  
271 combined great circle-fixed point mean direction as the reference pole. VGP latitudes reveal the  
272 polarity changes in the section with positive/negative values indicating normal/reverse polarity (Fig.  
273 4). For specimens that display great circle trends, the point on the fitted great circle nearest the  
274 combined mean direction was used to calculate the VGP latitude (Hounslow et al., 2008). Major  
275 magnetozone normal and reverse couplets are labelled upward from the base of the section using  
276 the prefix SCH (Shichuanhe), with polarity magnetozone pairs comprising a lower predominantly  
277 normal-polarity (“N”) and an overlying reversed-polarity “R”. Intervals denoted by lowest quality  
278 and poorly defined directions (e.g., S3, T3 and X), are indicated with a gray bar to display  
279 uncertainly. Seven main magnetozones, from SCH1 to SCH7, are based on at least three successive  
280 specimens with consistent polarity. Also present are a number of tentative submagnetozones (less  
281 than full width bars marked as .1r, .1n etc.), defined by a single specimen with acceptable quality  
282 (Fig. 4).

283

### 284 **5. Discussion**

#### 285 **5.1 Permian–Triassic boundary magnetostratigraphy in North China**

286 The Permian–Triassic Boundary occurs in normal magnetochron LT1n, a position which has been

287 well documented in both marine and non-marine successions (Hounslow and Balabanov, 2018 and  
288 references therein). At the Induan Global Boundary Stratotype Section and Point (GSSP) in Meishan,  
289 South China, the base of the Triassic is marked by the first occurrence (FO) of the conodont  
290 *Hindeodus parvus* in Bed 27c (Yin et al., 2001). However, magnetostratigraphic studies from  
291 Meishan display poor inter-study consistency, thus the exact relationship between the FO of *H.*  
292 *parvus* and the boundaries of magnetozone LT1n are unclear in the GSSP (Hounslow and Muttoni,  
293 2010; Zhang et al., 2021). At the Shangsi section, the base of magnetozone LT1n coincides with  
294 the base of the Feixianguan Formation (base of bed 28), within the *Clarkina meishanensis* conodont  
295 zone, which was estimated at  $252.23 \pm 0.08$  Ma using a Monte Carlo statistical method (Yuan et al.,  
296 2019; Fig. 6 and 7). This is similar to the  $252.2 \pm 0.23$  Ma age for the base of LT1n estimated using  
297 Bayesian methods in Hounslow and Balabanov (2018). Hence, at the SCH section, magnetozone  
298 SCH3n is equivalent to magnetozone LT1n, based on our new age of  $252.21 \pm 0.15$  Ma obtained  
299 from an ash bed 3.5 m below the base of SCH3n (Fig. 6). Given the latest calibration of the PTB at  
300  $251.902 \pm 0.024$  Ma based on U-Pb CA-ID-TIMS geochronology (Burgess et al., 2014), this latest  
301 Changhsingian date provides independent, radioisotopic evidence to establish a robust PTB  
302 magnetostratigraphic framework for North China. The comparative age and the polarity stratigraphy  
303 indicate that the base of LT1n is a synchronous marker useful for global correlation, occurring ca.  
304 0.3 Ma prior to the PTB (Fig. 7).

305 The correlation is also supported by biostratigraphic evidence from the mixed marine-  
306 terrestrial biota found at SCH. This fauna consists of a terrestrial spinicaudatan (conchostracan)  
307 *Euestheria gutta-Magniesteria mangaliensis-Palaeolimnadiopsis vilujensis* assemblage and the  
308 marine bivalve *Pteria variabilis*, which is found about 1 m above the base of magnetozone SCH3n.

309 This fauna is akin to the mixed terrestrial-marine biota in South China, which appears immediately  
310 after the demise of the Late Permian *Gigantopteris* flora (Chu et al., 2019). The *Euestheria gutta*  
311 assemblage with co-preserved specific marine bivalves has also been considered an important  
312 marker for the Permian–Triassic transitional beds (Chu et al., 2019). A similar spinicaudatan fauna  
313 (*Euestheria gutta-Palaeolimnadiopsis vilujensis* assemblage) was also recognized in the lower  
314 Buntsandstein coeval with the Central German Composite magnetozone interval CG3n–4n, which  
315 is equivalent to magnetochron LT1n (Szurlies, 2007, 2013; Scholze et al., 2017; Fig. 6).

316 Compiled data from many marine carbonate successions have indicated that the major  
317 minimum in  $\delta^{13}\text{C}_{\text{carb}}$  was around the PTB (e.g., Korte and Kozur, 2010), and falling within the lower  
318 part of LT1n (Shen et al., 2019; Zhang et al., 2021). Such carbon isotopic excursions have also been  
319 suggested to be nearly synchronous with the changes in  $\delta^{13}\text{C}_{\text{org}}$  in terrestrial facies (Wu et al., 2021b).  
320 Thus, by combining the magnetostratigraphy and geochronology with the organic carbon isotope  
321 curve (Wu et al., 2020), the PTB at SCH is estimated to occur at a level about 8 m higher than the  
322 base of magnetozone SCH3n, around the largest negative excursion in  $\delta^{13}\text{C}_{\text{org}}$ , within the upper part  
323 of the middle Sunjiagou Formation (Fig. 7). Additionally, our new magnetostratigraphic data also  
324 allows a better constraint for the onset of the carbon isotope excursion (CIE) during the latest  
325 Permian. This was previously suggested to be located at ~27 m below the base of SCH3n on the  
326 basis of purely chemostratigraphic considerations (Wu et al., 2020), but is now placed ~3 m below  
327 the base of SCH3n, within the upper part of magnetozone SCH2r (i.e., magnetochron LP3r; Fig. 7).

328 Our results are also in good agreement with the age-constrained magnetostratigraphy from  
329 the Sydney Basin, eastern Australia. The Permian–Triassic transition of the Sydney Basin contains  
330 three normal magnetozones, with normal magnetozone C2n first detected in the base of the Coalcliff

331 Sandstone (Belica, 2017; Fig. 7). The radioisotopic ages from the basal Bulli Coal (Metcalf et al.,  
332 2015) and basal Coalcliff Sandstone (Fielding et al., 2019, 2021) allow a robust correlation of  
333 magnetozone C2n with LT1n. However, the position of the base of magnetozone C2n is unclear,  
334 since there is a ~3.5 m unsampled interval covering the underlying Bulli Coal bed (Fig. 7).

335 The Permian–Triassic magnetostratigraphy from the Karoo Basin, South Africa is equivocal.  
336 The integrated magnetic polarity stratigraphy of Ward et al. (2005) showed two reverse-to-normal  
337 couplets. The longer normal magnetozone of the lower couplet, has its base slightly preceding the  
338 vertebrate turnover, with an associated negative  $\delta^{13}\text{C}_{\text{carb}}$  excursion, which was suggested equivalent  
339 with magnetozone LT1n. However, this situation has not been confirmed by subsequently studies.  
340 The *Daptocephalus*–*Lystrosaurus* transition is mostly within a normal magnetozone (see summaries  
341 in Gastaldo et al., 2021), which is, coupled to a U-Pb ID-TIMS age of 253.48 Ma from ~60 m below  
342 the vertebrate-defined PTB and is so considered to be early Changshingian (Gastaldo et al., 2015).  
343 This inconsistency could either be due to a local hiatus (Gastaldo et al. 2015) or difficulties in  
344 isolating the primary magnetization from the Jurassic partial remagnetization (Belica, 2017).

345 Correlation of magnetozone interval SCH1–SCH2 to the GPTS is not straightforward due to  
346 the lack of supporting fossil markers within this interval. Also, intrabasinal correlation with the  
347 nearby Hancheng section at this level is difficult owing to the infrequent magnetostratigraphic  
348 sampling, which defines magnetozone O1 (Ma et al., 1992; Fig. 6). Overall, the relative thickness  
349 of magnetozones SCH1n–SCH2r are similar to magnetozone interval CG1n–CG2r in the Central  
350 German Composite (Szurlics, 2013; Fig. 6). In the Germanic Basin, magnetozones CG1n and CG2n  
351 were correlated to magnetozones IRA1n and IRA2n from the Abadeh section (Fig. 6), corresponding  
352 to the late Wuchiapingian and early Changhsingian on the basis of the conodonts (*Merrillina*



353 *divergens* and *Mesogondolella britannica*) and Re-Os dating from the Zechstein successions  
354 (Szurlies, 2013; Fig. 6). However, these conodonts occur throughout the Lopingian and fail to  
355 provide a precise timescale (Henderson and Mei, 2000). Instead, magnetozone CG1n has been  
356 correlated to magnetochron LP2n.3n (equivalent to IRA2n), with its upper boundary at ca. 253.2  
357 Ma, within the *Clarkina subcarinata* conodont zone at the Abadeh section and probably within the  
358 *C. changxingensis* zone at Shangsi (Hounslow and Balabanov, 2018). Accordingly, magnetozone  
359 SCH1n is tentatively correlated to magnetochron LP2n.3n and SCH2n to LP3n (Fig. 6).

360

## 361 **5.2 Lower Triassic magnetostratigraphy in North China**

362 The two reference polarity scales for the remainder of the Lower Triassic, that from Buntsandstein  
363 (Szurlies, 2007, 2013) and the marine composite GPTS (Hounslow and Muttoni, 2010), are  
364 generally similar, but show a few differences in number and relative duration of the briefer  
365 magnetochrons (Fig. 6). The placement of the Induan–Olenekian Boundary (IOB) in the  
366 Buntsandstein composite also has some divergences of interpretation (Szurlies, 2007; Hounslow  
367 and Muttoni, 2010). In China, the IOB is informally defined by the FAD of *Novispathodus waageni*  
368 s.l. at West Pingdingshan section, ~2.5 m from the top of reverse magnetozone WP4r and equivalent  
369 to the topmost part of magnetochron LT2r (Sun et al., 2009; Fig. 6). The *Densioisporites nejburgii*  
370 palynological assemblage from the Middle Buntsandstein, spans the late Dienerian to Smithian,  
371 suggesting that the IOB in Central Germany is within the lower part of the Middle Buntsandstein  
372 (Kürschner and Herrgreen, 2010; Fig. 6), suggesting that CG6n is the equivalent to LT3n in the  
373 GPTS (orange correlation box in Fig. 6).

374 At SCH, the reverse polarity dominated interval SCH3r–SCH5r is correlated to the dominantly

375 reverse magnetochron interval LT1r–LT4r and CG4r–CG7r, spanning the mid-Griesbachian to mid-  
376 Smithian (Fig. 6). Correlation to the same lithostratigraphic interval at Hancheng section reveals  
377 much similarity in the number and relative thickness of magnetozones. Crucially there are two major  
378 normal polarity magnetozones (SCH4n and SCH5n) with a third tentative normal submagnetozone  
379 SCH5r.1n in this interval at SCH, likely to that in the GPTS and Buntsandstein Composite which  
380 also have three normal magnetozones. The wide sample spacing at Hancheng has probably missed  
381 the upper normal polarity magnetozone (SCH5r.1n) seen at SCH (Fig. 6). Overall, the relative  
382 thickness of magnetozones in the SCH3r–SCH5r is most similar to the Buntsandstein composite in  
383 the CG4r–CG7r interval. Thus, the IOB at SCH is placed at the base of SCH5n in the Lower part of  
384 the Liujiagou Formation (Fig. 6). However, a hiatus could be present given that there is an abrupt  
385 change in depositional environments from the shallow lacustrine facies of the Sunjiagou Formation  
386 to the overlying channelized, conglomeratic sandstones of the basal Liujiagou Formation. As a result,  
387 magnetozone SCH4n could be the equivalent of LT3n and SCH5n =LT4n. This would suggest that  
388 magnetochron LT2 is missing.

389 Like the underlying magnetozone interval SCH4r–SCH5, the succeeding thick normal SCH6n  
390 is more like the CG8n to CG10n interval in the Central German composite, than the marine-based  
391 magnetochrons LT5n to LT9n (Fig. 6), which range in age from the mid Smithian to late Spathian  
392 (Hounslow and Muttoni, 2010). Four reverse magnetozones within the LT5n–LT9n interval occur  
393 in arctic Canadian and Norwegian sections (Ogg and Steiner, 1991; Hounslow et al., 2008), but their  
394 thicknesses differ greatly compared to the equivalent interval in the Central German Composite.  
395 Notably, only two major reverse magnetozones (but 6 submagnetozones) were recovered from this  
396 interval at the Majiashan section (South China; Li et al., 2016; Fig. 6). At Majiashan, the

397 cyclostratigraphically-calibrated polarity stratigraphy can be readily matched with the Central  
398 German Composite, providing important constraints for marine to non-marine correlations (Li et al.,  
399 2016; Fig. 6). No major reverse polarity magnetozones were detected within SCH6n, but three  
400 tentative submagnetozones SCH6n.1r–SCH6n.3r were detected (Fig. 4). However, in the nearby  
401 Hancheng section, reverse magnetozones O4r and O5r, straddling the Liujiagou and Heshanggou  
402 formations, were recognized (Ma et al., 1992; Fig. 6). The absence of such major reverse  
403 magnetozones at SCH could be related to local erosional loss. Sparse flora assigned to the  
404 *Pleuromeia sternbergii* assemblage in SCH6n interval suggests an Olenekian age (Wang and Wang,  
405 1990), consistent with the magnetostratigraphic results. The Smithian–Spathian transition is marked  
406 by consistent normal polarity in arctic Canada, arctic Norway and South China, an interval which  
407 is likely condensed in the upper part of magnetochron LT6n due to a major boreal transgression  
408 (Ogg and Steiner, 1991; Hounslow et al., 2008; Li et al., 2016). It is likely that the well-defined  
409 reverse magnetozones O4r and O5r in Hancheng are equivalent to magnetozones MJ1r and MJ2r at  
410 Majiashan and LT6r–LT8r, CG8r–CG9n.2r in the reference sections (marked with blue correlated  
411 interval in Fig. 6). Hence the base of the Spathian is interpreted to be in the middle of SCH6n, in  
412 the uppermost of the Liujiagou Formation at SCH (Fig. 6).

413 Magnetozone SCH6r represents the late Spathian magnetochron LT9r and CG10r from the  
414 Buntsandstein (Fig. 6). This late Spathian reverse magnetochron has been widely recognized and  
415 contains at least one normal submagnetochron (Hounslow and Muttoni, 2010). Only normal polarity  
416 is found in the overlying Ermaying Formation (SCH7n or upper part of O6n) and is likely correlative  
417 to MT3n of the early Anisian (Fig. 6). The formational boundary is represented by a distinct  
418 sedimentary facies switch: the conglomeratic fluvial sandstones of the basal Ermaying Formation

419 resting with erosional contact on the underlying red lacustrine siltstone-dominated Heshanggou  
420 Formation (Supplementary Fig. S1). The absence of the equivalent of magnetozone SCH6r in  
421 Hancheng was likely due to complete removal of the upper most Spathian LT9r. The brief  
422 magnetochrons MT1–2 of the GPTS, which characterize the Olenekian–Anisian transition, appear  
423 to be missing in many Chinese sections, and in other continental successions (Hounslow and  
424 Muttoni, 2010). The occurrence of the *Sinokannemeyeria* fauna and a CA-ID-TIMS U-Pb age  
425 ( $243.528 \pm 0.069$  Ma), unequivocally place the Ermaying Formation within the Middle Triassic (Liu  
426 et al., 2018). Moreover, a diverse spinicaudatan *Protimonocarina-Euestheria* assemblage found in  
427 the lowermost part of the Ermaying Formation indicates an early Middle Triassic age (Wu, 1991).  
428 Accordingly, the base of the Anisian is placed within the hiatus between the Heshanggou and  
429 Ermaying formations, with magnetochrons MT1 and MT2 being removed at the hiatus.

430

### 431 **5.3 Magnetostratigraphic implications for the timing of the end-Permian terrestrial crisis in** 432 **North China**

433 The Permian–Triassic GSSP section at Meishan is thought to record two pulses of marine biotic  
434 extinctions (Song et al., 2013) at  $251.941 \pm 0.037$  Ma and  $251.880 \pm 0.031$  Ma (Burgess et al., 2014),  
435 all within the lower part of LT1n and its equivalents (Zhang et al., 2021; Fig. 7). At Shangsi, the  
436 distinctive changeover of conodonts from *Clarkina*-dominated to *Hindeodus*-dominated faunas (FO  
437 of *Hindeodus changxingensis*) marks the extinction interval, starting in bed 28a, within the lower  
438 part of magnetochron LT1n (Glen et al., 2007; Yuan et al., 2019; Fig. 7).

439 The timing of the terrestrial ecological crisis has been constrained by absolute ages or high-  
440 resolution chemostratigraphy (Fielding et al., 2019, 2021; Chu et al., 2020; Gastaldo et al., 2020).

441 Detailed sedimentological investigations in the Sydney Basin (eastern Australia), have  
442 demonstrated that the Permian–Triassic transitional sequences are stratigraphically complete,  
443 recording the disappearance of the *Glossopteris* flora within the top of the Bulli Coal (Fielding et  
444 al., 2019, 2021). The floral turnover occurred ~160–600 kyrs before the marine biotic crisis,  
445 according to several ID-TIMS ages from the basal Bulli Coal and basal Coalcliff Sandstone  
446 (Fielding et al., 2019, 2021). However, the relationship between the extinction interval and magnetic  
447 polarity cannot be precisely confirmed owing to the sampling gap in the coal bed (Fig. 7). In North  
448 China, collapse of terrestrial palaeofloras was marked by the extinction of approximately 54% of  
449 plant genera within the Sunjiagou Formation (Chu et al. 2019). This floral extinction slightly  
450 predated the latest Permian negative carbon-isotope excursion (Wu et al., 2020), and falls in  
451 magnetozone SCH2r (equivalent to magnetochron LP3r, immediately below LT1n; Fig. 7).  
452 According to our proposed magnetostratigraphic correlations, corroborated by our new absolute age  
453 ( $252.21 \pm 0.15$  Ma), collapse of plant communities occurred about  $270 \pm 150$  kyrs earlier than the  
454 marine extinction (Fig. 7). Hence, our new magnetostratigraphic framework provides additional  
455 independent evidence that the terrestrial ecological crisis started before the marine mass extinction.

456

## 457 **6 Conclusion**

458 A detailed magnetostratigraphic investigation, spanning the early Changhsingian to early Anisian,  
459 was undertaken at the continental Shichuanhe section, yielding the first detailed Early Triassic non-  
460 marine timescale in North China. Results from the ~300 m thick red-bed dominated sequence  
461 exhibit dual polarity magnetizations, with the magnetic remanence mainly carried by hematite. The  
462 antipodal distributed directions are statistically undistinguishable to those expected in the Early

463 Triassic (Yang et al., 1991), pass the reversal test, and indicate a paleolatitude for the Shichuanhe  
464 section of 18.1°N.

465 Seven main magnetozones are recognized and the relative thickness of magnetozones displays  
466 good similarity, particularly to the composite from the Buntsandstein (Fig. 6). A new Late Permian  
467 CA-ID-TIMS U-Pb age of 252.21±0.15 Ma, provides direct evidence for the correlation of  
468 magnetozones SCH3n at Shichuanhe to magnetochron LT1n of the GPTS. According to our multi-  
469 disciplinary approach, the PTB is placed at ca. 8 m above the base of SCH3n, around the minimum  
470 of a negative  $\delta^{13}\text{C}_{\text{org}}$  excursion, within the middle part of the Sunjiagou Formation. The  
471 spinicaudatan fauna within SCH3n is identical to that found in Central Germany within  
472 magnetozones CG3n–CG4n (equivalent to LT1n), adding additional paleontological support for our  
473 correlations. According to our composite magnetostratigraphy, base of the Olenekian is placed in  
474 the lower part of the Liujiagou Formation (base of SCH5n) and the Smithian–Spathian boundary in  
475 the upper part of the Liujiagou Formation. Combined magnetic polarity and sedimentary facies  
476 analysis reveal that the Spathian–Anisian transitional strata are absent.

477 With respect to the polarity timescale, destabilization of the terrestrial ecosystem in North  
478 China during the Permian–Triassic transition started within the upper part of magnetochron LP3r,  
479 270±150 kyrs before the onset of the marine crisis, which falls within the base of the overlying  
480 normal magnetochron LT1n. The Shichuanhe section has preserves a complete terrestrial Permian–  
481 Triassic boundary record and is an important reference section for terrestrial and marine  
482 stratigraphic correlation.

483

484 **Acknowledgements**

485           We thank Yingchao Xu and Yiming Ma for the help in paleomagnetic data analysis. We also  
486 thank Haijun Song, Wenchao Shu, Kaixuan Ji, Yuyang Wu and Gan Liu for the invaluable advice in  
487 stratigraphic correlation and discussions about the PTME on land. This work was supported by the  
488 National Natural Science Foundation of China [grant number 41530104, 41661134047, 42030513],  
489 and the UK Natural Environment Research Council's Eco-PT Project (NE/P0137724/1), which is  
490 part of the Biosphere Evolution, Transitions and Resilience (BETR) Program.

491

492   Supplementary material

493   Supplementary file A, B, C

494

495   **References**

496

1

2 **References**

3 Benton, M.J., 2018. Hyperthermal-driven mass extinctions: killing models during the Permian–  
4 Triassic mass extinction. *Philosophical Transactions of the Royal Society A: Mathematical,*  
5 *Physical and Engineering Sciences* 376, 20170076. <https://doi.org/10.1098/rsta.2017.0076>.

6 Burgess, S.D., Bowring, S., Shen, S.Z., 2014. High-precision timeline for Earth’s most severe  
7 extinction. *Proceedings of the National Academy of Sciences* 111, 3316–3321.  
8 <https://doi.org/10.1073/pnas.1317692111>.

9 Burgess, S.D., Bowring, S.A., 2015. High-precision geochronology confirms voluminous  
10 magmatism before, during, and after Earth’s most severe extinction. *Science Advances* 1,  
11 e1500470. DOI: 10.1126/sciadv.1500470.

12 Cao, Y., Song, H.Y., Algeo, T.J., Chu, D.L., Du, Y., Tian, L., Wang, Y.H., Tong, J.N., 2019.  
13 Intensified chemical weathering during the Permian–Triassic transition recorded in terrestrial  
14 and marine successions. *Palaeogeography, Palaeoclimatology, Palaeoecology* 519, 166–177.  
15 <https://doi.org/10.1016/j.palaeo.2018.06.012>.

16 Chu, D.L., Tong, J.N., Benton, M.J., Yu, J.X., Huang, Y.F., 2019. Mixed continental-marine biotas  
17 following the Permian–Triassic mass extinction in South and North China. *Palaeogeography,*  
18 *Palaeoclimatology, Palaeoecology* 519, 95–107. <https://doi.org/10.1016/j.palaeo.2017.10.028>.

19 Chu, D.L., Grasby, S.E., Song, H.J., Dal Corso, J., Wang, Y., Mather, T.A., Wu, Y.Y., Song, H.Y.,  
20 Shu, W.C., Tong, J.N., Wignall, P.B., 2020. Ecological disturbance in tropical peatlands prior  
21 to marine Permian–Triassic mass extinction: *Geology* 48, 288–292,  
22 <https://doi.org/10.1130/G46631.1>.



23 Chu, D.L., Dal Corso, J., Shu, W.C., Song, H.J., Wignall, P.B., Grasby, S.E., van de Schootbrugge,  
24 B., Zong, K.Q., Wu, Y.Y., Tong, J.N., 2021. Metal-induced stress in survivor plants following  
25 the end-Permian collapse of land ecosystems. *Geology*. <https://doi.org/10.1130/G48333.1>.

26 Davydov, V.I., Karasev, E.V., Nurgalieva, N.G., Schmitz, M.D., Budnikov, I.V., Biakov, A.S.,  
27 Kuzina, D.M., Silantiev, V.V., Urazaeva, M.N., Zharinova, V.V., Zorina, S.O., Gareev, B.,  
28 Vasilenko, D.V., 2021. Climate and biotic evolution during the Permian–Triassic transition in  
29 the temperate Northern Hemisphere, Kuznetsk Basin, Siberia, Russia. *Palaeogeography,*  
30 *Palaeoclimatology, Palaeoecology*, 110432. <https://doi.org/10.1016/j.palaeo.2021.110432>.

31 Fan, J.X., Shen, S.Z., Erwin, D.H., Sadler, P.M., MacLeod, N., Cheng, Q.M., Hou, X.D., Yang, J.,  
32 Wang, X.D., Wang, Y., Zhang, H., Chen, X., Li, G.X., Zhang, Y.C., Shi, Y.K., Yuan, D.X., Chen,  
33 Q., Zhang, L.N., Li, C., Zhao, Y.Y., 2020. A high-resolution summary of Cambrian to Early  
34 Triassic marine invertebrate biodiversity. *Science* 367, 272–277. DOI:  
35 10.1126/science.aax4953.

36 Feng, Z., Wei, H.B., Guo, Y., He, X.Y., Sui, Q., Zhou, Y., Liu, H.Y., Gou, X.D., Lv, Y., 2020. From  
37 rainforest to herbland: New insights into land plant responses to the end-Permian mass  
38 extinction. *Earth-Science Reviews*, 103153. <https://doi.org/10.1016/j.earscirev.2020.103153>.

39 Fetisova, A.M., Veselovskii, R.V., Latyshev, A.V., Rad'ko, V.A., Pavlov, V.E., 2014. Magnetic  
40 stratigraphy of the Permian–Triassic traps in the Kotui River valley (Siberian Platform): New  
41 paleomagnetic data. *Stratigraphy and Geological Correlation* 22, 377–390.  
42 <https://doi.org/10.1134/S0869593814040054>.

43 Fielding, C.R., Frank, T.D., McLoughlin, S., Vajda, V., Mays, C., Tevyaw, A.P., Winguth, A.,  
44 Winguth, C., Nicoll, R.S., Bocking, M., Crowley, J.L., 2019. Age and pattern of the southern

45 high-latitude continental end-Permian extinction constrained by multiproxy analysis. *Nature*  
46 *Communications* 10, 385, <https://doi.org/10.1038/s41467-018-07934-z>.

47 Gallet, Y., Krystyn, L., Besse, J., Saidi, A., Ricou, L.E., 2000. New constraints on the Upper Permian  
48 and Lower Triassic geomagnetic polarity timescale from the Abadeh section (central Iran).  
49 *Journal of Geophysical Research: Solid Earth* 105, 2805–2815.  
50 <https://doi.org/10.1029/1999JB900218>.

51 Gastaldo, R.A., Kamo, S.L., Neveling, J., Geissman, J.W., Bamford, M., Looy, C.V., 2015. Is the  
52 vertebrate-defined Permian–Triassic boundary in the Karoo Basin, South Africa, the terrestrial  
53 expression of the end-Permian marine event? *Geology* 43, 939–942.

54 Gastaldo, R.A., Neveling, J., Geissman, J.W., Kamo, S.L., 2018. A lithostratigraphic and  
55 magnetostratigraphic framework in a geochronologic context for a purported Permian–Triassic  
56 boundary section at Old (West) Lootsberg Pass, Karoo Basin, South Africa. *Geological Society*  
57 *of America Bulletin* 130, 1411–1438. <https://doi.org/10.1130/B31881.1>.

58 Gastaldo, R.A., Neveling, J., Geissman, J.W., Looy, C.V., 2019. Testing the *Daptocephalus* and  
59 *Lystraosaurus* assemblage zones in a lithostratigraphic, magnetostratigraphic, and  
60 palunological framework in the Free state, South Africa. *Palaios* 34, 542–561.  
61 <https://doi.org/10.2110/palo.2019.019>.

62 Gastaldo, R.A., Kamo, S.L., Neveling, J., Geissman, J.W., Looy, C.V., Martini, A.M., 2020. The  
63 base of the *Lystrosaurus* Assemblage Zone, Karoo Basin, predates the end-Permian marine  
64 extinction. *Nature Communications* 11, 1428. <https://doi.org/10.1038/s41467-020-15243-7>.

65 Grădinaru, E., Orchard, M.J., Nicora, A., Gallet, Y., Besse, J., Krystyn, L., Sobolev, E.S., Atudorei,  
66 N., Ivanova, D., 2007. The global boundary stratotype section and point (GSSP) for the base

67 of the Anisian stage: Deşli Caira Hill, North Dobrogea, Romania. *Albertiana* 36, 54–71.

68 Guo, W.W., Tong, J.N., Tian, L., Chu, D.L., Bottjer, D.J., Shu, W.C., Ji, K.X., 2019. Secular  
69 variations of ichnofossils from the terrestrial Late Permian–Middle Triassic succession at the  
70 Shichuanhe section in Shaanxi Province, North China. *Global and Planetary Change* 181,  
71 102978. <https://doi.org/10.1016/j.gloplacha.2019.102978>.

72 Hounslow, M.W., 2006. PMagTools version 4.2—a tool for analysis of 2D and 3D directional data.  
73 <http://dx.doi.org/10.13140/RG.2.2.19872.58880>.

74 Hounslow, M.W., Balabanov, Y.P., 2018. A geomagnetic polarity timescale for the Permian,  
75 calibrated to stage boundaries. *Geological Society, London, Special Publications* 450, 61–103.

76 Hounslow, M.W., Muttoni, G., 2010. The geomagnetic polarity timescale for the Triassic: linkage  
77 to stage boundary definitions, in: Lucas, S.G. (Ed.), *Triassic Timescale*, 61–102.

78 Hounslow, M.W., Peters, C., Mork, A., Weitschat, W., Vigran, J.O., 2008. Biomagnetostratigraphy  
79 of the Vikinghogda Formation, Svalbard (Arctic Norway), and the geomagnetic polarity  
80 timescale for the Lower Triassic. *Geological Society of America Bulletin* 120, 1305–1325.  
81 <https://doi.org/10.1130/B26103.1>.

82 Huang, B.C., Yan, Y.G., Piper, J.D.A., Zhang, D.H., Yi, Z.Y., Yu, S., Zhou, T.H., 2018.  
83 Paleomagnetic constraints on the paleogeography of the East Asian blocks during Late  
84 Paleozoic and Early Mesozoic times. *Earth-Science Reviews* 186, 8–36.  
85 <https://doi.org/10.1016/j.earscirev.2018.02.004>.

86 IGCCS (Institute of Geology Chinese Academy of Geological Sciences), 1980. Mesozoic  
87 stratigraphy and paleontology of Shanganning Basin (I). Geological Publishing House, Beijing,  
88 pp. 1–212 [in Chinese].

89 Jaffey, A.H., Flynn, K.F., Glendenin, L.E., Bentley, W.C., Essling, A.M., 1971. Precision  
90 measurement of half-lives and specific activities of  $^{235}\text{U}$  and  $^{238}\text{U}$ . *Physical review C* 4, 1889–  
91 1906. DOI: <https://doi.org/10.1103/PhysRevC.4.1889>.

92 Ji, K.X., Wignall, P.B., Peakall, J., Tong, J.N., Chu, D.L., Pruss, S.B., 2021. Unusual intraclast  
93 conglomerates in a stormy, hot-house lake: The Early Triassic North China Basin.  
94 *Sedimentology*. doi: 10.1111/sed.12903.

95 Kamo, S.L., Czamanske, G.K., Krogh, T.E., 1996. A minimum U-Pb age for Siberian flood-basalt  
96 volcanism. *Geochimica et Cosmochimica Acta* 60, 3505–3511. [https://doi.org/10.1016/0016-](https://doi.org/10.1016/0016-7037(96)00173-1)  
97 [7037\(96\)00173-1](https://doi.org/10.1016/0016-7037(96)00173-1).

98 Korte, C., Kozur, H.W., 2010. Carbon-isotope stratigraphy across the Permian–Triassic boundary:  
99 A review. *Journal of Asian Earth Sciences* 39, 215–235.  
100 <https://doi.org/10.1016/j.jseaes.2010.01.005>.

101 Kürschner, W.M., Herngreen, G.W., 2010. Triassic palynology of central and northwestern Europe:  
102 a review of palynofloral diversity patterns and biostratigraphic subdivisions. *Geological*  
103 *Society, London, Special Publications* 334, 263–283. <https://doi.org/10.1144/SP334.11>.

104 Lehrmann, D.J., Ramezani, J., Bowring, S.A., Martin, M.W., Montgomery, P., Enos, P., Payne, J.L.,  
105 Orchard, M.J., Hongmei, W., Jiayong, W., 2006. Timing of recovery from the end-Permian  
106 extinction: Geochronologic and biostratigraphic constraints from south China. *Geology* 34,  
107 1053–1056. <https://doi.org/10.1130/G22827A.1>.

108 Li, M.S., Ogg, J., Zhang, Y., Huang, C.J., Hinnov, L., Chen, Z.Q., Zou, Z.Y., 2016. Astronomical  
109 tuning of the end-Permian extinction and the Early Triassic Epoch of South China and Germany.  
110 *Earth and Planetary Science Letters* 441, 10–25. <https://doi.org/10.1016/j.epsl.2016.02.017>.

111 Liu, J., Ramezani, J., Li, L., Shang, Q., Xu, G., Wang, Y., Yang, J., 2018. High-precision temporal  
112 calibration of Middle Triassic vertebrate biostratigraphy: U-Pb zircon constraints for the  
113 *Sinokannemeyeria* Fauna and *Yonghesuchus*. *Vertebrata Palasiatica* 55, 1–9.  
114 <https://doi.org/10.19615/j.cnki.1000-3118.170808>.

115 Liu, X.C., Wang, W., Shen, S.Z., Gorgij, M.N., Ye, F.C., Zhang, Y.C., Furuyama, S., Kano, A., Chen,  
116 X.Z., 2013. Late Guadalupian to Lopingian (Permian) carbon and strontium isotopic  
117 chemostratigraphy in the Abadeh section, central Iran. *Gondwana Research* 24, 222–232.  
118 <https://doi.org/10.1016/j.gr.2012.10.012>.

119 Lu, J., Zhang, P., Yang, M., Shao, L., Hilton, J., 2020. Continental records of organic carbon isotopic  
120 composition ( $\delta^{13}\text{C}_{\text{org}}$ ), weathering, paleoclimate and wildfire linked to the End-Permian Mass  
121 Extinction. *Chemical Geology* 558, 119764. <https://doi.org/10.1016/j.chemgeo.2020.119764>.

122 Lurcock, P.C., Wilson, G.S., 2012. PuffinPlot: A versatile, user-friendly program for paleomagnetic  
123 analysis. *Geochemistry, Geophysics, Geosystems* 13, Q06Z45, doi:10.1029/2012GC004098.

124 Ma, X.H., Xing, L.S., Yang, Z.Y., Xu, S.J., Zhang, J.X., 1992. Paleomagnetic study since late  
125 Paleozoic in the Ordos basin, Seismological Press, Beijing, pp. 1–99 [in Chinese].

126 Meng, Q.R., Wu, G.L., Fan, L.G., Wei, H.H., 2019. Tectonic evolution of early Mesozoic  
127 sedimentary basins in the North China block. *Earth-science reviews* 190, 416–438.  
128 <https://doi.org/10.1016/j.earscirev.2018.12.003>.

129 McFadden, P.L., McElhinny, M.W., 1988. The combined analysis of remagnetization circles and  
130 direct observations in palaeomagnetism. *Earth and Planetary Science Letters* 87, 161–172.  
131 [https://doi.org/10.1016/0012-821X\(88\)90072-6](https://doi.org/10.1016/0012-821X(88)90072-6).

132 McFadden, P.L., McElhinny, M.W., 1990. Classification of the reversal test in palaeomagnetism.

133 Geophysical Journal International 103, 725–729. <https://doi.org/10.1111/j.1365->  
134 246X.1990.tb05683.x.

135 Ogg, J.G., Steiner, M.B., 1991. Early Triassic magnetic polarity time scale-integration of  
136 magnetostratigraphy, ammonite zonation and sequence stratigraphy from stratotype sections  
137 (Canadian Arctic Archipelago). *Earth and Planetary Science Letters* 107, 69–89.  
138 [https://doi.org/10.1016/0012-821X\(91\)90044-I](https://doi.org/10.1016/0012-821X(91)90044-I).

139 Ouyang, S., Zhang, Z., 1982. Early Triassic palynological assemblage in Dengfeng, northwestern  
140 Henan. *Acta Palaeontol. Sin.* 21, 685–696 [in Chinese with English abstract].

141 Payne, J.L., Turchyn, A.V., Paytan, A., DePaolo, D.J., Lehrmann, D.J., Yu, M., Wei, J., 2010.  
142 Calcium isotope constraints on the end-Permian mass extinction. *Proceedings of the National*  
143 *Academy of Sciences* 107, 8543–8548. <https://doi.org/10.1073/pnas.0914065107>.

144 Ramezani, J., Hoke, G.D., Fastovsky, D.E., Bowring, A.S., Therrien, F., Dworkin, S.I., Atchley, S.C.,  
145 Nordt, L.C., 2011. High-precision U-Pb zircon geochronology of the Late Triassic Chinle  
146 Formation, Petrified Forest National Park (Arizona, USA): Temporal constraints on the early  
147 evolution of dinosaurs. *GSA Bulletin* 123: 2142–2159. <https://doi.org/10.1130/B30433.1>.

148 Scholze, F., Wang, X., Kirscher, U., Kraft, J., Schneider, J.W., Götz, A.E., Joachimski, M.M.,  
149 Bachtadse, V., 2017. A multistratigraphic approach to pinpoint the Permian–Triassic boundary  
150 in continental deposits: The Zechstein–Lower Buntsandstein transition in Germany. *Global and*  
151 *Planetary Change* 152, 129–151. <https://doi.org/10.1016/j.gloplacha.2017.03.004>.

152 Shen, S.Z., Crowley, J.L., Wang, Y., Bowring, S.A., Erwin, D.H., Sadler, P.M., Cao, C.Q., Rothman,  
153 D.H., Henderson, C.M., Ramezani, J., 2011. Calibrating the end-Permian mass extinction.  
154 *Science* 334, 1367–1372. DOI: 10.1126/science.1213454.

155 Song, H., Wignall, P.B., Tong, J., Yin, H., 2013. Two pulses of extinction during the Permian–  
156 Triassic crisis. *Nature Geoscience* 6, 52–56. <https://doi.org/10.1038/ngeo1649>.

157 Song, H.J., Wignall, P.B., Dunhill, A.M., 2018. Decoupled taxonomic and ecological recoveries  
158 from the Permo–Triassic extinction. *Sci Adv* 4, eaat5091. DOI: 10.1126/sciadv.aat5091.

159 Steiner, M.B., 2006. The magnetic polarity time scale across the Permian–Triassic boundary.  
160 Geological Society, London, Special Publications 265, 15–38.  
161 <https://doi.org/10.1144/GSL.SP.2006.265.01.02>.

162 Sun, Y.D., Joachimski, M.M., Wignall, P.B., Yan, C.B., Chen, Y.L., Jiang, H.S., Wang, L.N., Lai,  
163 X.L., 2012. Lethally hot temperatures during the Early Triassic greenhouse. *Science* 338, 366–  
164 370. DOI: 10.1126/science.1224126.

165 Sun, Z.M., Hounslow, M.W., Pei, J.L., Zhao, L.S., Tong, J.N., Ogg, J.G., 2009. Magnetostratigraphy  
166 of the Lower Triassic beds from Chaohu (China) and its implications for the Induan–Olenekian  
167 stage boundary. *Earth and Planetary Science Letters* 279, 350–361.  
168 <https://doi.org/10.1016/j.epsl.2009.01.009>.

169 Szurlies, M., 2007. Latest Permian to Middle Triassic cyclo-magnetostratigraphy from the Central  
170 European Basin, Germany: Implications for the geomagnetic polarity timescale. *Earth and*  
171 *Planetary Science Letters* 261, 602–619. <https://doi.org/10.1016/j.epsl.2007.07.018>.

172 Szurlies, M., 2013. Late Permian (Zechstein) magnetostratigraphy in Western and Central Europe.  
173 Geological Society, London, Special Publications 376, 73–85. <https://doi.org/10.1144/SP376.7>.

174 Tong, J.N., Chu, D.L., Liang, L., Shu, W.C., Song, H.J., Song, T., Song, H.Y., Wu, Y.Y., 2019.  
175 Triassic integrative stratigraphy and timescale of China. *Science China (Earth Sciences)* 62,  
176 189–222. <https://doi.org/10.1007/s11430-018-9278-0>.

177 Wang, Z.Q., Wang, L.X., 1982. A new species of the lycopsid *Pleuromeia jiaochengensis* from the  
178 Early Triassic of Shanxi, China and its ecology. *Palaeontology* 25, 215–226.

179 Wang, Z.Q., Wang, L.X., 1990. New plant assemblages from the bottom of the Mid-Triassic  
180 Ermaying Formation. *Shanxi Geology* 5, 303–318 [in Chinese with English abstract].

181 Ward, P.D., Botha, J., Buick, R., De Kock, M.O., Erwin, D.H., Garrison, G.H., Kirschvink, J.L.,  
182 Smith, R., 2005. Abrupt and Gradual Extinction Among Late Permian Land Vertebrates in the  
183 Karoo Basin, South Africa. *Science* 307, 709–714. DOI: 10.1126/science.1107068.

184 Wignall, P.B., 2015, *The Worst of Times: How Life on Earth Survived Eighty Million Years of*  
185 *Extinction*: Princeton, New Jersey, Princeton University Press, pp. 1–224.

186 World Magnetic Model 2019–2024;  
187 <https://www.ngdc.noaa.gov/geomag/calculators/magcalc.shtml#igrfwmm>.

188 Wu, T.Y., 1991. Conchostracan assemblage from bottom of Ermaying Formation, Shaanxi. 30, 631–  
189 642. [in Chinese with English abstract].

190 Wu, Y.Y., Tong, J.N., Algeo, T.J., Chu, D.L., Cui, Y., Song, H.Y., Shu, W.C., Du, Y., 2020. Organic  
191 carbon isotopes in terrestrial Permian-Triassic boundary sections of North China: Implications  
192 for global carbon cycle perturbations. *Geological Society of America Bulletin* 132, 1106–1118.  
193 <https://doi.org/10.1130/B35228.1>.

194 Wu, Y.Y., Chu, D.L., Tong, J.N., Song, H.J., Dal Corso, J., Wignall, P.B., Song, H.Y., Du, Y., Cui,  
195 Y., 2021. Six-fold increase of atmospheric pCO<sub>2</sub> during the Permian–Triassic mass extinction.  
196 *Nature Communications* 12, 2137. <https://doi.org/10.1038/s41467-021-22298-7>.

197 Yang, Z.Y., Ma, X.H., Besse, J., Courtillot, V., Xing, L.S., Xu, S.J., Zhang, J.X., 1991.  
198 Paleomagnetic results from Triassic sections in the Ordos Basin, North China. *Earth and*



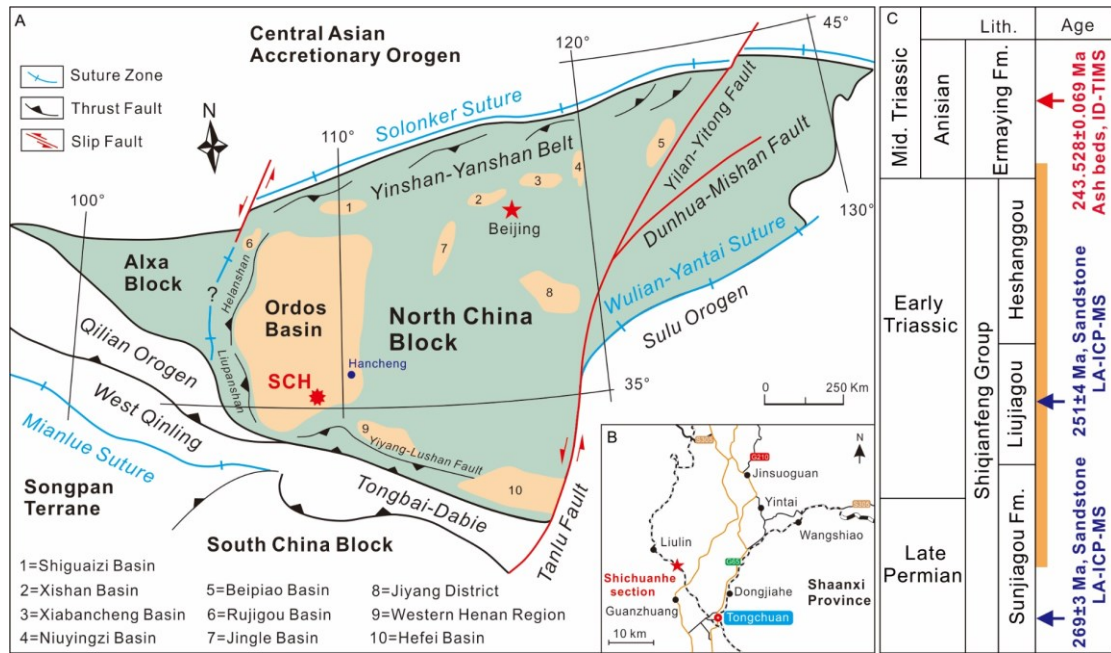
199 Planetary Science Letters 104, 258–277. [https://doi.org/10.1016/0012-821X\(91\)90208-Y](https://doi.org/10.1016/0012-821X(91)90208-Y).

200 Yin, H.F., Zhang, K.X., Tong, J.N., Yang, Z.Y., Wu, S.B., 2001. The global stratotype section and  
201 point (GSSP) of the Permian–Triassic boundary. *Episodes* 24, 102–114.

202 Yuan, D.X., Shen, S.Z., Henderson, C.M., Chen, J., Zhang, H., Zheng, Q.F., Wu, H.C., 2019.  
203 Integrative timescale for the Lopingian (Late Permian): A review and update from Shangsi,  
204 South China. *Earth-Science Reviews* 188, 190–209.  
205 <https://doi.org/10.1016/j.earscirev.2018.11.002>.

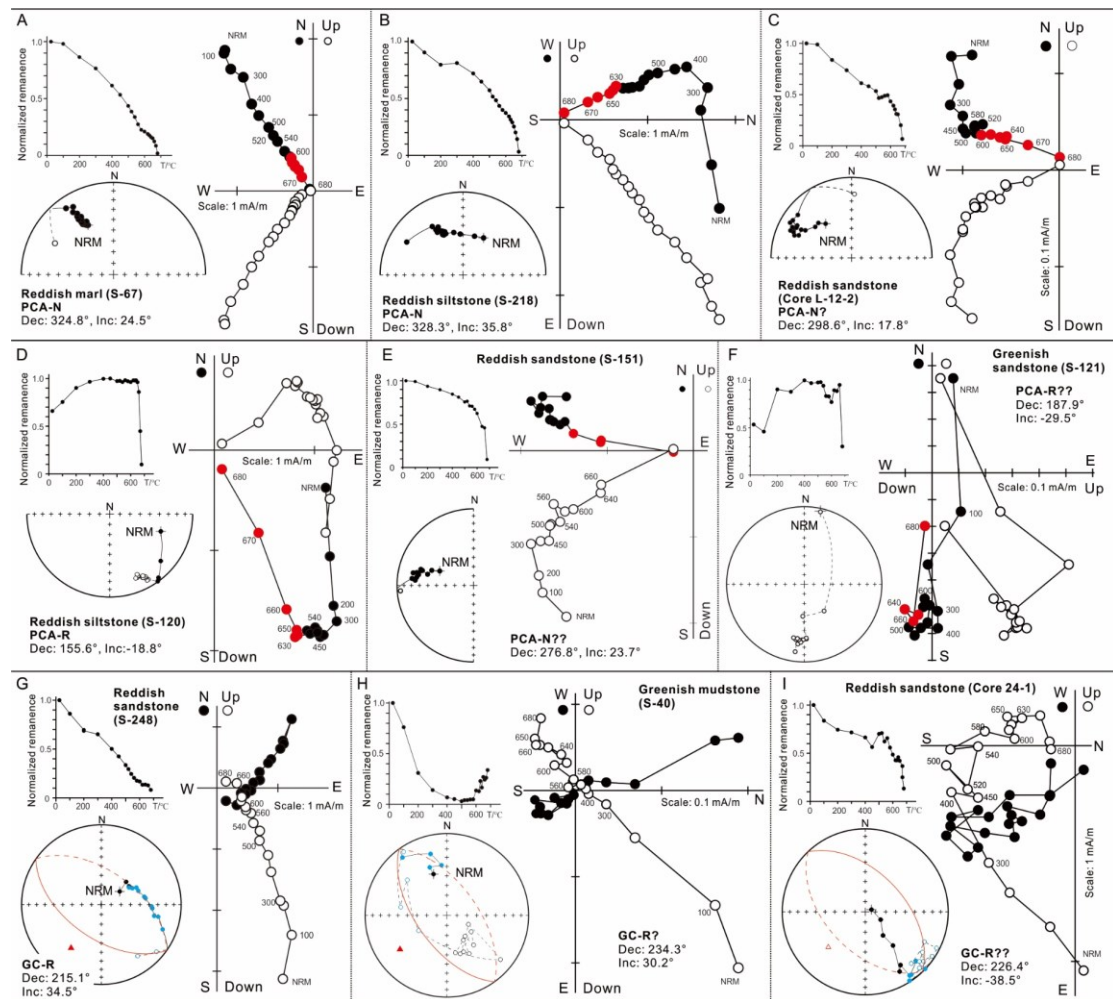
206 Zhang, M., Qin, H.F., He, K., Hou, Y.F., Zheng, Q.F., Deng, C.L., He, Y., Shen, S.Z., Zhu, R.X.,  
207 Pan, Y.X., 2021. Magnetostratigraphy across the end-Permian mass extinction event from the  
208 Meishan sections, southeastern China. *Geology*. <https://doi.org/10.1130/G49072.1>.

209 Zhu, R.K., Xu, H.X., Deng, S.W., Guo, H.L., 2007. Lithofacies palaeogeography of the Permian in  
210 northern China. *J. Palaeogeogr* 9, 133–142 [in Chinese with English abstract].



1  
2 Fig 1. Simplified paleotectonic map of the North China Block and its sedimentary basins (modified  
3 from Meng et al., 2019). Red star marks the studied Shichuanhe (SCH) section. Blue point indicates  
4 the Hancheng section. Inset B shows a detailed location of the SCH section. C. Brief Permian–  
5 Triassic chrono- and lithostratigraphic framework in North China. ID-TIMS age is from Liu et al.  
6 (2018), LA-ICP-MS ages are from Zhu et al. (2019). Orange bar represents studied interval.

7



8

9

Fig 2. Representative demagnetization behaviors with polarity interpretation of specimens from

10

Shichuanhe section. A–F: Principal Component Analysis (PCA), steps used for ChRM line-fits are

11

highlighted in red. A. A largely single component magnetization shows a stable end-point that is

12

close to expected Early Triassic direction in North China (polarity N; S1 class), Sunjiagou

13

Formation. B. After removal of an eastward LTC below 400°C, specimen shows good linearity to

14

the origin with the ChRM from 630–680°C steps, polarity N (S1), Heshangou Formation. C.

15

Similar demagnetization behavior to B, but the ChRM direction is a little deviated from expected

16

direction (N?, S2), Liujiagou Formation. D. Two component magnetizations with the ChRM 630°C

17

to the origin (R, S1). Apparent mid-stable component is from blocking temperature overlap between

18

the ChRM and the LTC, Sunjiagou Formation. E. Specimen shows good linearity above 600°C, but

19

isolated ChRM is deviated from expected direction (N??, S3), Liujiagou Formation. F. The last three

20

steps show moderately linear ChRM component and the LTC is a composite LTC and Triassic

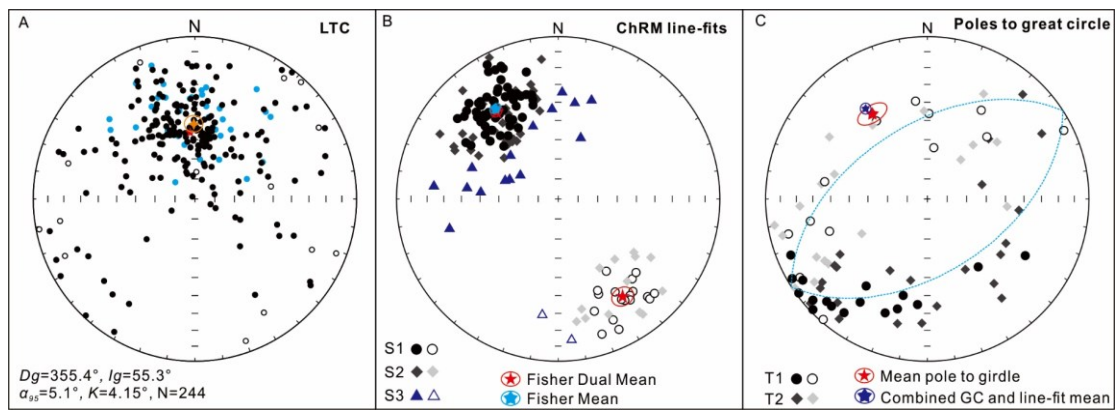
21

reverse component (R??, S3), Sunjiagou Formation. Filled (open) symbols are lower (upper)

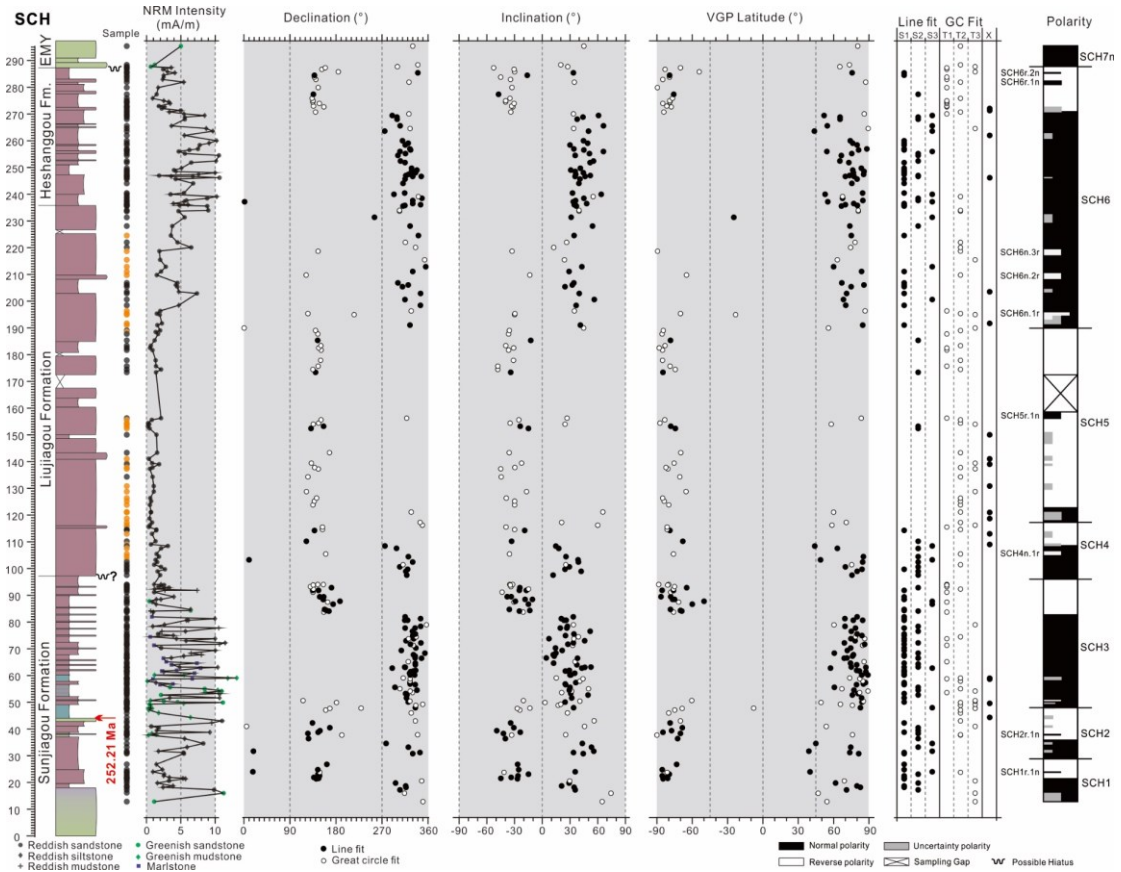
22

hemisphere. G–I: Great-circle (GC) fits, red arc represents fitted great circle and blue indicates

23 points used. Lower projection paths dashed and upper projection paths are solid. G. Great circle  
 24 plane from 200–680°C, specimen shows unscattered great circle trend towards the expected reverse  
 25 direction (R, T1). LTC (100–500°C) is likely a composite component, Heshanggou Formation. H.  
 26 Well-defined LTC 100–400 °C and a somewhat scattered trend (moderate arc length 100–540°C)  
 27 towards Triassic reverse, with erratic directions above 600°C, due to thermal alteration (R?, T2),  
 28 Sunjiagou Formation. I. Well-defined LTC NRM–400°C and a trend towards expected Triassic  
 29 reverse direction with the great circle fitted to the higher temperature steps (R??, T3), Liujiagou  
 30 Formation.  
 31



32  
 33 Fig 3. Equal-area stereographic projection of the low-temperature components (LTC) and  
 34 characteristic (ChRM) components of the Shichuanhe section. A. LTC in geographic coordinates,  
 35 with the Fisher means (red star) close to the recent geomagnetic dipole field direction (orange star)  
 36 at the SCH site (IGRF, computed from  
 37 <https://www.ngdc.noaa.gov/geomag/calculators/magcalc.shtml#igrfwmm>). B. Dual polarity ChRM  
 38 line fits (in stratigraphic coordinates), with calculated Fisher (dual) mean (only S1 and S2 data used)  
 39 and Fisher means of all converted to normal (Blue star with 95% confidence ellipse). C. Poles to  
 40 the great circle planes of T1 and T2 class data, along with the mean of the combined great circle and  
 41 line-fits (McFadden and McElhinny, 1988). The single girdle plane (dotted) is the plane normal to  
 42 the mean direction calculated using both the great circle poles and ChRM fits. Red star indicates the  
 43 mean pole to the great circle girdle of points and its elliptical 95% confidence cone. The filled (open)  
 44 circles refer to the lower (upper) hemisphere, respectively.



46

47 Fig 4. Magnetostratigraphy of the Shichuanhe (SCH) section with polarity quality ratings.

48 Demagnetization behavior of S and T refer to ChRM line-fits (filled circles) and great circle fits

49 (open circles), respectively, which are subdivided into S1, S2, S3 and T1, T2, T3 class (see text for

50 details). Specimens with no Triassic magnetization are marked X. Half-width bars indicate a single

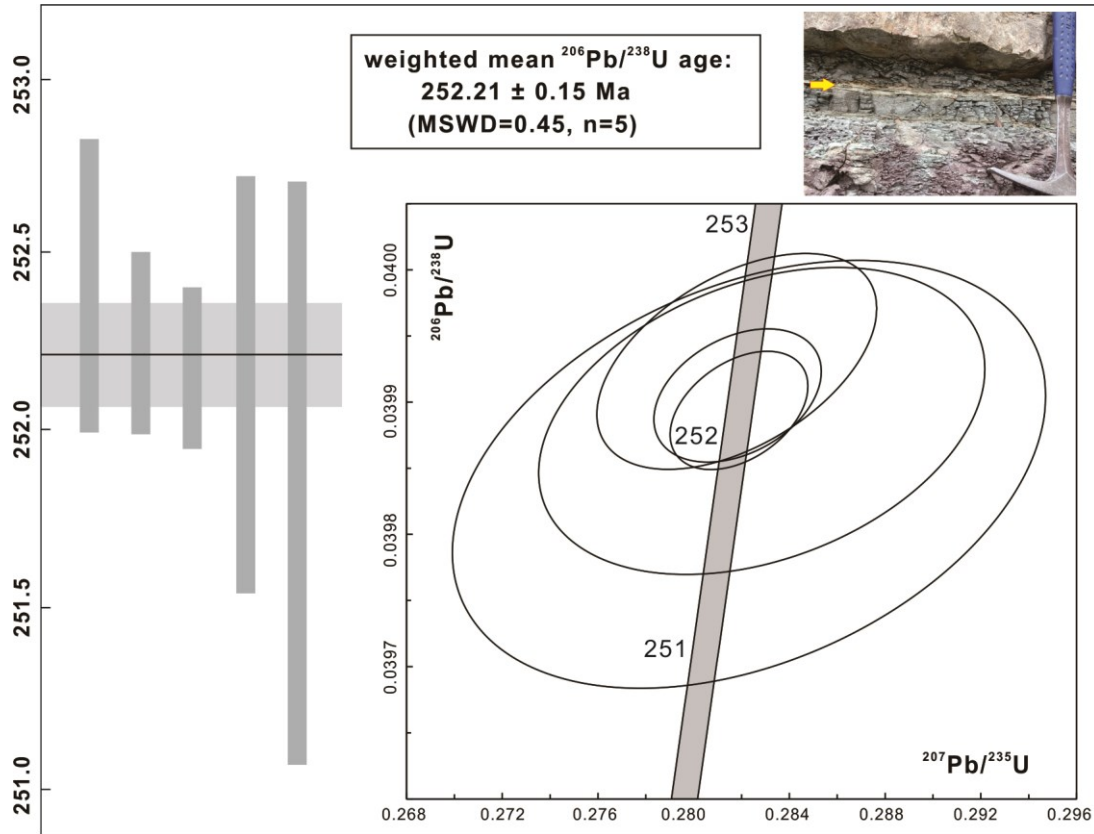
51 sample with high quality (S1, S2 or T1, T2), showing opposite polarity interpretation with respect

52 to adjacent samples. For the gray bar, one-quarter-width means single poorest quality or

53 undetermined polarity (S3, T3 and X), whereas half-width indicates successive poorest or

54 undetermined polarities.

55



56

57 Fig 5. Concordia diagram and ranked  $^{206}\text{Pb}/^{238}\text{U}$  plot analyzed zircon grains from the Shichuanhe  
 58 ash bed (upper right inset marked by yellow arrow). Each vertical bar represents a single zircon  
 59 analysis included in the weighted mean age and the bar height is proportional to the  $2\sigma$  analytical  
 60 uncertainty. The horizontal black line and grey bar represent the calculated weighted mean age and  
 61 its  $2\sigma$  analytical uncertainty envelope, respectively. Outliers excluded from age calculation plot  
 62 outside the diagram area are not shown herein.

63

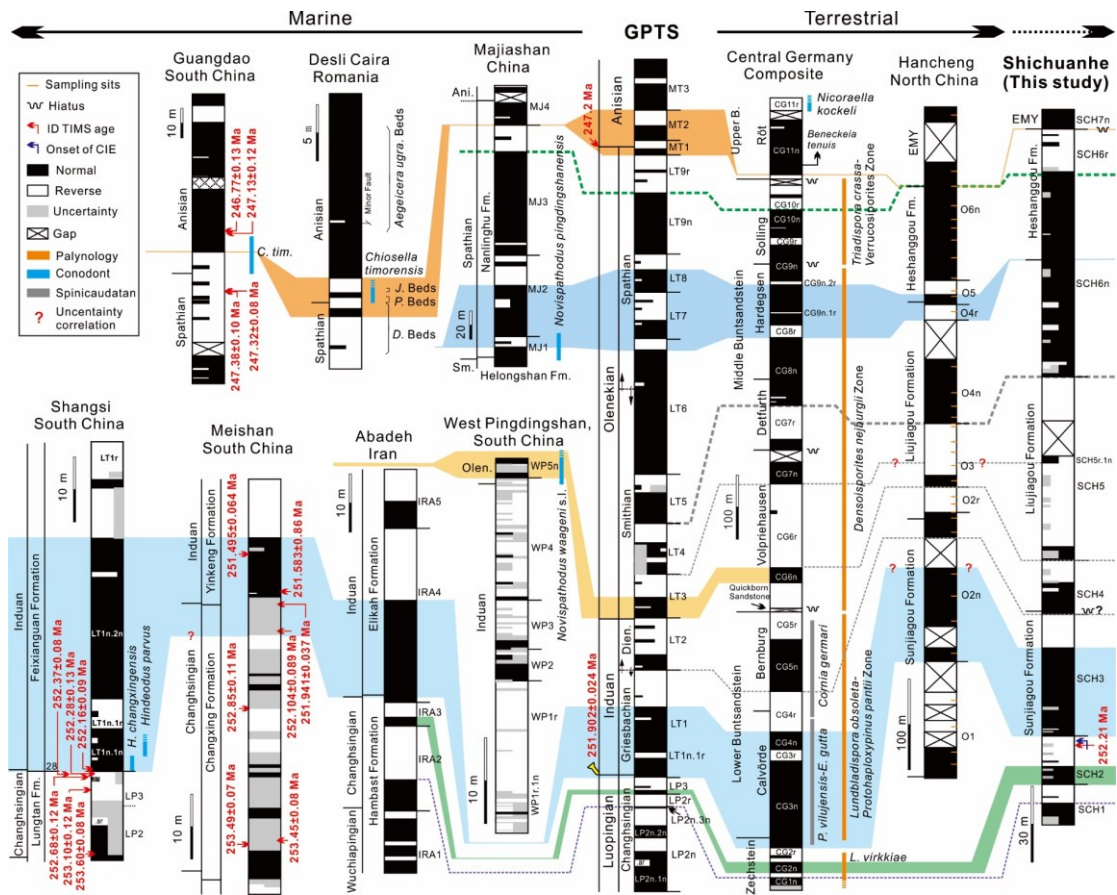
		Mean site direction ( $^{\circ}$ )							Reversal test ( $G_r/G_c$ )	Virtual Geomagnetic Pole (VGP) ( $^{\circ}$ )			
	Polarity	$D_g$	$I_g$	$D_s$	$I_s$	$K_s$	$\alpha_{95}$	N		Lat.	Long.	$\delta p/\delta m$	Paleolat.
<b>Shichuanhe section (Tongchuan)</b>													
Line fit <sup>§</sup>	Normal	324.9	39.0	325.0	34.0	26.54	2.9	93					
	Reverse	145.1	-33.9	146.4	-28.5	28.31	4.9	31					
	All	324.9	37.7	325.4	32.6	26.54	2.5	124	Rb (5.67/5.74)*	54.7	358.6	1.60/2.84	17.7 N
GC fit <sup>¶</sup>	All	328.6	44.2	327.3	37.0	16.36	4.2	73					
Combined <sup>†</sup>	Normal	325.5	39.6	325.6	34.1	24.14	2.7	118					
	Reverse	145.4	-37.2	145.7	-32.3	21.19	3.5	79					
	All	325.5	38.4	325.6	33.3	14.30	1.9	197	Ra (1.82/4.38)*	55.2	359.0	1.23/2.16	18.1 N
<b>Hancheng (Yang et al., 1991)</b>													
Line fit <sup>§</sup>	Normal	334.7	34.3	334.2	30.0	114.8	4.8	9 (sites)		61.2	349.5		
	Reverse	160.2	-32.5	156.4	-31.7	48.8	8.7	7 (sites)		62.1	345.2		
	All	337.1	33.5	335.2	32.5	76.7	4.2	16 (sites)	Rb (2.54/8.82)*	61.7	347.6		17.6 N
<b>Tongchuan, LJG (Ma et al., 1992)</b>													
Line fit <sup>§</sup>	All	330.1	43.2	329.7	32.4	165	6.0	5 (sites)		58.0	354.1	3.8/6.8	17.6 N

<sup>§</sup>: conventional Fisher mean. # : Great Circle mean. + : Combined line fit and great circle fit (McFadden and McFadden, 1988).  $D_s$ ,  $I_s$  and  $D_g$ ,  $I_g$ : declination and inclination in geographic and stratigraphic coordinates, respectively.  $K_s$ : precision parameter after tilt correction.  $\alpha_{95}$ : half-angle of cone of 95% confidence about the mean direction in stratigraphic coordinate. N: number used to calculate the mean direction. Lat. and Long.: latitude and longitude of the mean virtual geomagnetic pole, respectively.  $\delta p/\delta m$ : semi-axes of the 95% confidence level ellipse on palaeomagnetic pole. Paleolat.: calculated paleolatitude.  
<sup>¶</sup> Reversal test (McFadden and McElhinny, 1990).  $G_r$  is the angular separation between the inverted reverse and normal directions and  $G_c$  is the critical value for the reverse test. In the reversal test,  $G_r/G_c$ , marked \* suggest a common K value.  $R_r$  and  $R_n$  mean positive reversal test with critical angle that  $R_r < 5^{\circ}$  and  $R_n < 10^{\circ}$ .

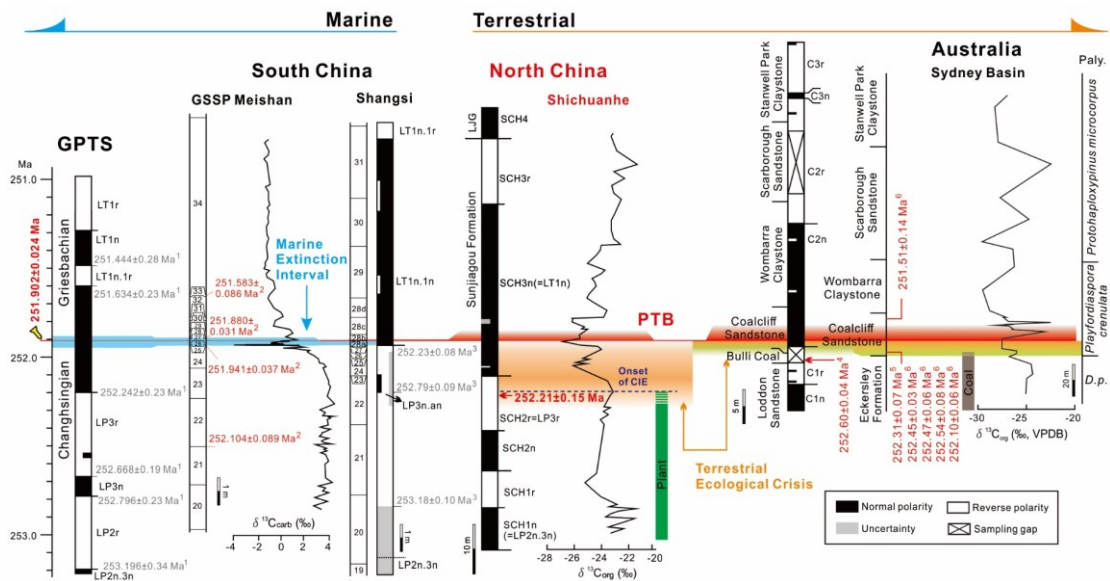
64

65 Table 1. Permian–Triassic mean directions and virtual geomagnetic poles for the Shichuanhe section  
 66 and other sections in North China. Paleolatitude and reversal test of Yang et al. (1991) were not  
 67 provided in the original study.

68



70 Fig 6. Changhsingian–Anisian magnetic polarity stratigraphy of North China and comparison with  
 71 other non-marine and marine successions. Geomagnetic polarity timescale (GPTS) is based on  
 72 Hounslow and Muttoni (2010) and Hounslow and Balabanov (2018). Compiled Central German  
 73 Composite and biostratigraphy (Szurlies, 2007, 2013; Kürschner and Hergreen, 2010; Scholze et  
 74 al., 2017). Hancheng section (Ma et al., 1992). Distance between sampling sites >30 m is marked  
 75 by a sampling gap. West Pingdingshan (Sun et al., 2009), Majiangshan (Li et al., 2016), Meishan  
 76 (Modified from Hounslow and Balabanov, 2018), Abadeh (Gallet et al., 2000; Szurlies, 2013),  
 77 Guangdao (Lehrmann et al., 2006), Shangsì (Hounslow and Balabanov, 2018; Yuan et al., 2019).  
 78 Desli Cairra (Grădinaru et al., 2007). Question marks indicate uncertain correlations. *D.*  
 79 *Beds*=*Deslicairites* Beds; *P. Beds*=*Paracrocordicera* Beds; *J. Beds*=*Japonites* Beds; *P. vilujensis*–  
 80 *E. gutta*=*Palaeolimnadiopsis vilujensis*–*Euetheria gutta*; *L. virkkiae*=*Lueckisporites virkkiae* Zone.



82

83 Fig 7. Correlation of the Permian–Triassic interval sequence at Shichuanhe with the GSSP at  
 84 Meishan (Burgess et al., 2014), Shangsì (Yuan et al., 2019) and Australian sections (Belica, 2017;  
 85 Fielding et al., 2019, 2021). Ages of <sup>1</sup>=calculated by Hounslow and Balabanov, 2018, <sup>2</sup>=Burgess et  
 86 al., 2014, <sup>3</sup>=calculated magnetozone boundary ages by Yuan et al., 2019, <sup>4</sup>=Metcalf et al., 2015,  
 87 <sup>5</sup>=Fielding et al., 2019, <sup>6</sup>=Fielding et al., 2021. GPTS is from (Hounslow and Balabanov, 2018).  
 88 Carbon isotope curve of Shichuanhe (Wu et al., 2020). Paly.=Palynostratigraphy (Mays et al., 2020).  
 89 *D.p.*=*Dulhuntyispora parvithola* Zone.



1 Supplementary Data A

2 This Supplementary data contains the following sections.

3 1. Sedimentology of the continental Shichuanhe Section (SCH)

4 Figure S1. Log of Shichuanhe section showing the lithology, sedimentary structures,  
5 depositional environments and the magnetic sampling positions

6 Figure S2. Photographs of the formation boundaries and representative sedimentary  
7 features of the Shichuanhe section.

8 2. Additional rock magnetic information

9 2.1 NRM intensity

10 Figure S3. Variations of NRM intensity with lithology

11 2.2 Thermomagnetic curve

12 Figure S4. Magnetic susceptibility versus temperature (K-T) curves of typical specimens

13

14 3. U-Pb geochronology methods and results

15 Figure S5. U-Pb dating results for zircons analyzed by LA-ICP-MS

16 4. Additional demagnetization data and palaeomagnetic mean directions

17 Figure S6–S10. Demagnetization behavior and the interpreted polarity of different  
18 lithologies

19 Table S1. Mean directions, reversal test and virtual geomagnetic poles for specimens with  
20 different quality-ratings.

21 5. Supplementary References

22

23

24

25

26

27

28

29

## 30 1. Sedimentology of the Shichuanhe Section (SCH)

31 Five facies associations (FAs) have been recognized at SCH, based on lithology, their stratigraphic  
32 packeting patterns, and physical sedimentary structures. More detailed sedimentological  
33 investigations in North China have been undertaken by Ji et al. (under review). Here we briefly  
34 represent the sedimentological feature throughout the SCH section (Fig. S2) and focus on the  
35 Permian–Triassic boundary sequence.

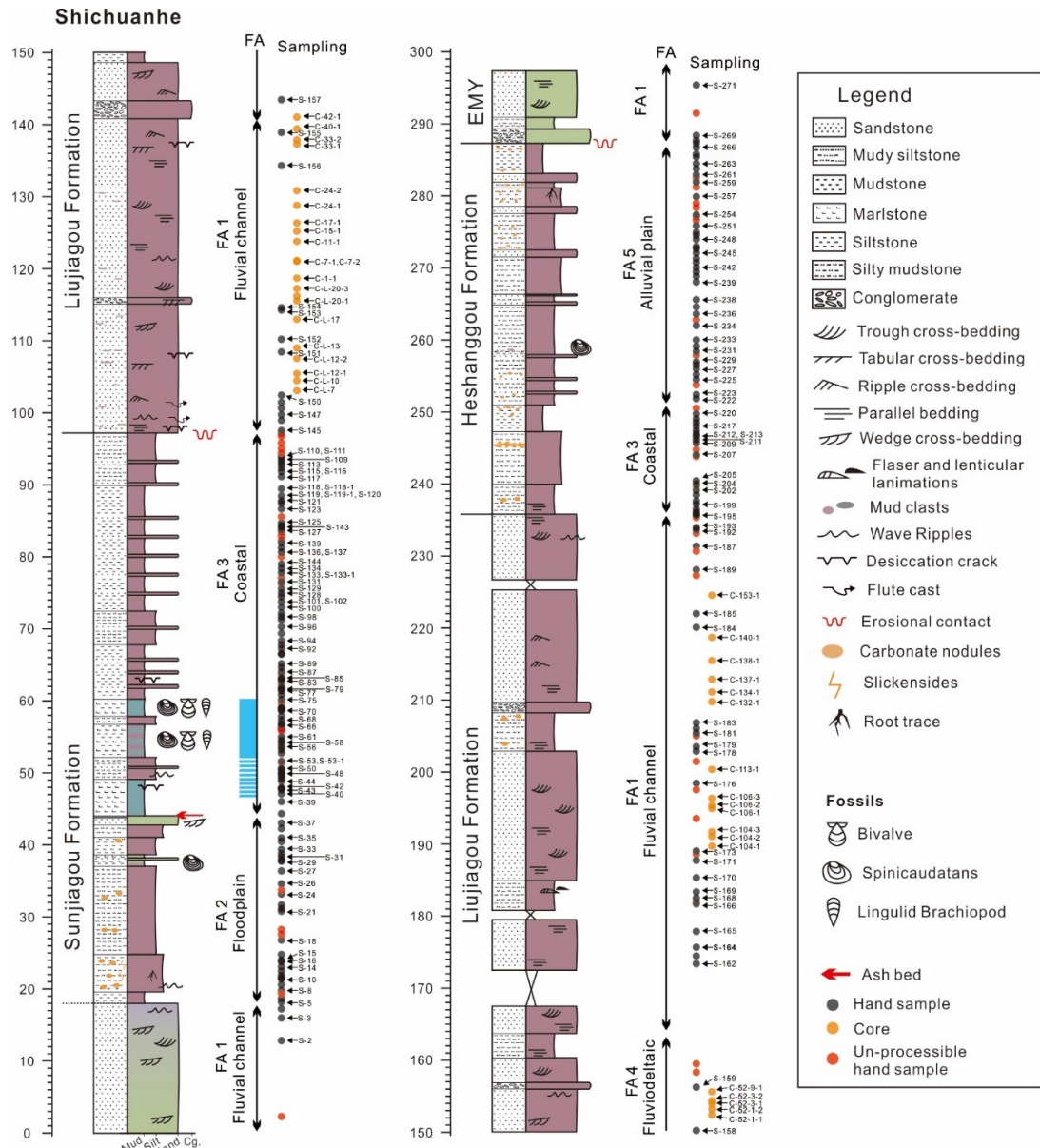
36 **FA1** is characterized by multistorey fine- to medium- grained sandstone up to 2 m thick,  
37 interbedded with thin red mudstones. This facies marks the lowermost and topmost parts of the  
38 section with green colored sandstones. This facies also forms the main part of the Liujiagou  
39 Formation with typical red coloration (Fig. S1). Trough and tabular cross-beddings and parallel  
40 laminations are common, ripple marks and desiccation cracks are occasionally present, especially  
41 in the lower Liujiagou Formation. Sand bodies in the basal Liujiagou Formation display slightly  
42 undulating but sharp contacts (Fig. S2E). Lag conglomerates of mudstone intraclasts are quite  
43 common (Fig. S2F) and flute casts preserved on the soles of sandstone beds are also found. The  
44 sharply bounded sandstones are stacked into lenticular channelized beds (Fig. S2G).

45 **FA2** consists of massive red mudstone, interbedded with thin rippled siltstones and paleosols are  
46 well-developed in this facies (including inceptisols succeeding aridisols), coupled with some root  
47 traces and burrows (Guo et al., 2019; Yu et al., 2022). This fine-grained facies is interpreted to be  
48 deposited under alluvial floodplain settings.

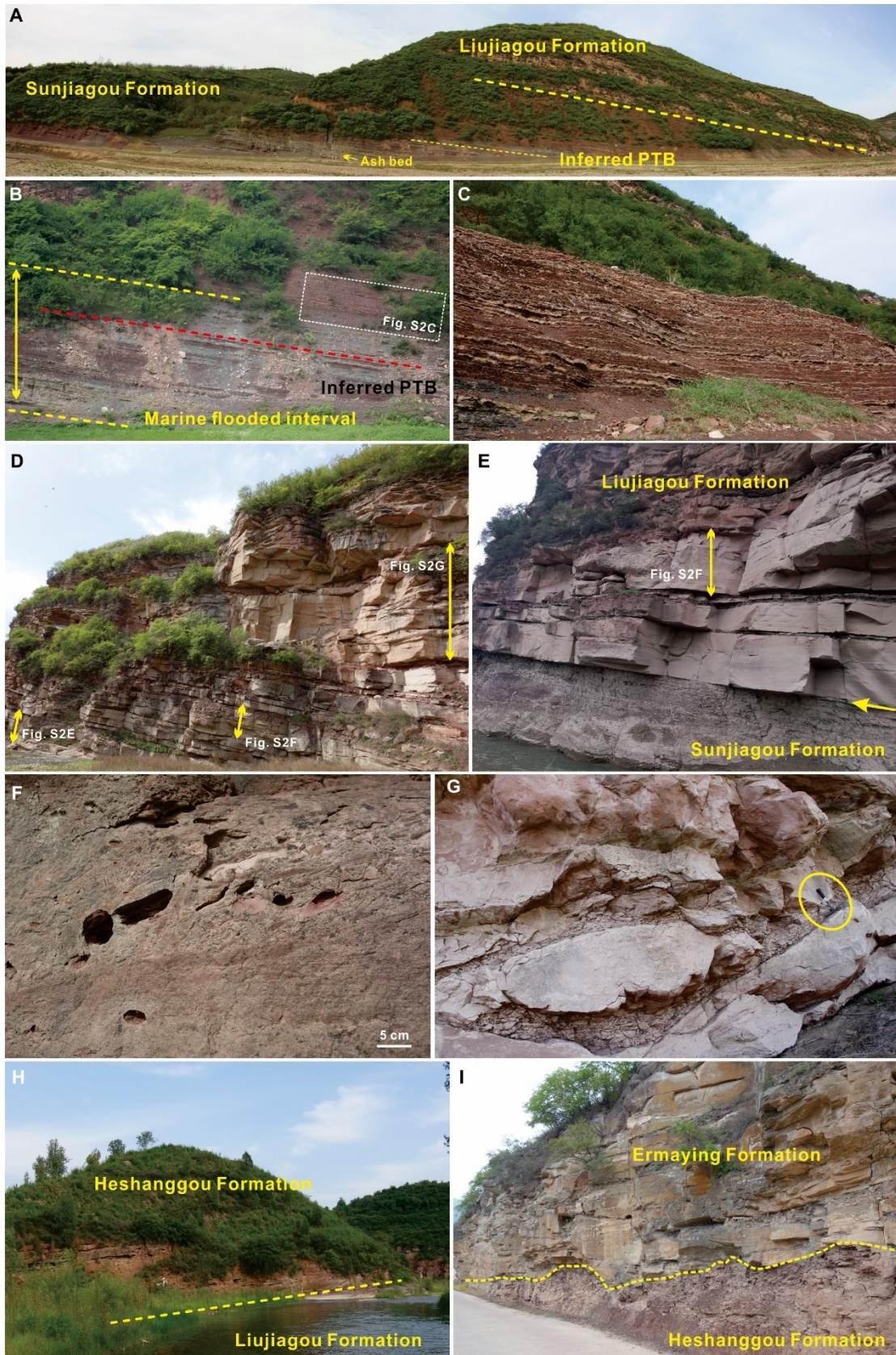
49 **FA3** is represented by alternating red, fine-grained calcareous sandstone and silty mudstone, with  
50 some marlstone interlayers (Fig. S2C), with occasional desiccation cracks and calcretes . This facies  
51 association is interpreted as formed in coastal environments (Ji et al., under review). Typically, the  
52 lower parts of FA3 in the section are characterized by green and red alternating mudstone and thin  
53 interbedded marlstones, and sandstones (Fig. S2B). These contain mixed terrestrial spinicaudatans  
54 and marine bivalves, which were affected by northeastwards directed regional marine transgressions  
55 (Chu et al., 2019). The inferred PTB lies in the upper part of this distinct interval.

56 **FA4** is distributed around the middle part of the Liujiagou formation, and is comprised of fine-  
57 grained sandstone and lenticular intraformational conglomerates, interleaved with dark red siltstone  
58 and mudstone. This facies association is formed in fluviodeltaic environments (Ji et al., under  
59 review).

60 **FA5** is represented by rhythmic alternations of sandstone up to 20–50 cm thick and massive siltstone,  
 61 with paleosols and trace fossils which are especially well developed in this interval (Yu et al., 2022).  
 62 **FA5** records an environment that was dominated by fine-grained deposition on alluvial plains, with  
 63 frequent subaerial exposure.  
 64



65  
 66 Figure S1. The Shichuanhe section showing lithology, sedimentary structures, depositional  
 67 environments and the paleomagnetic sampling positions. Blue bar on the facies association  
 68 represents an interval influenced by marine flooding .  
 69



70

71 Figure S2. Formation boundaries and representative sedimentary features of the Shichuanhe section.

72 A), Sunjiagou and the overlying Liujiagou formations with the inferred PTB and the

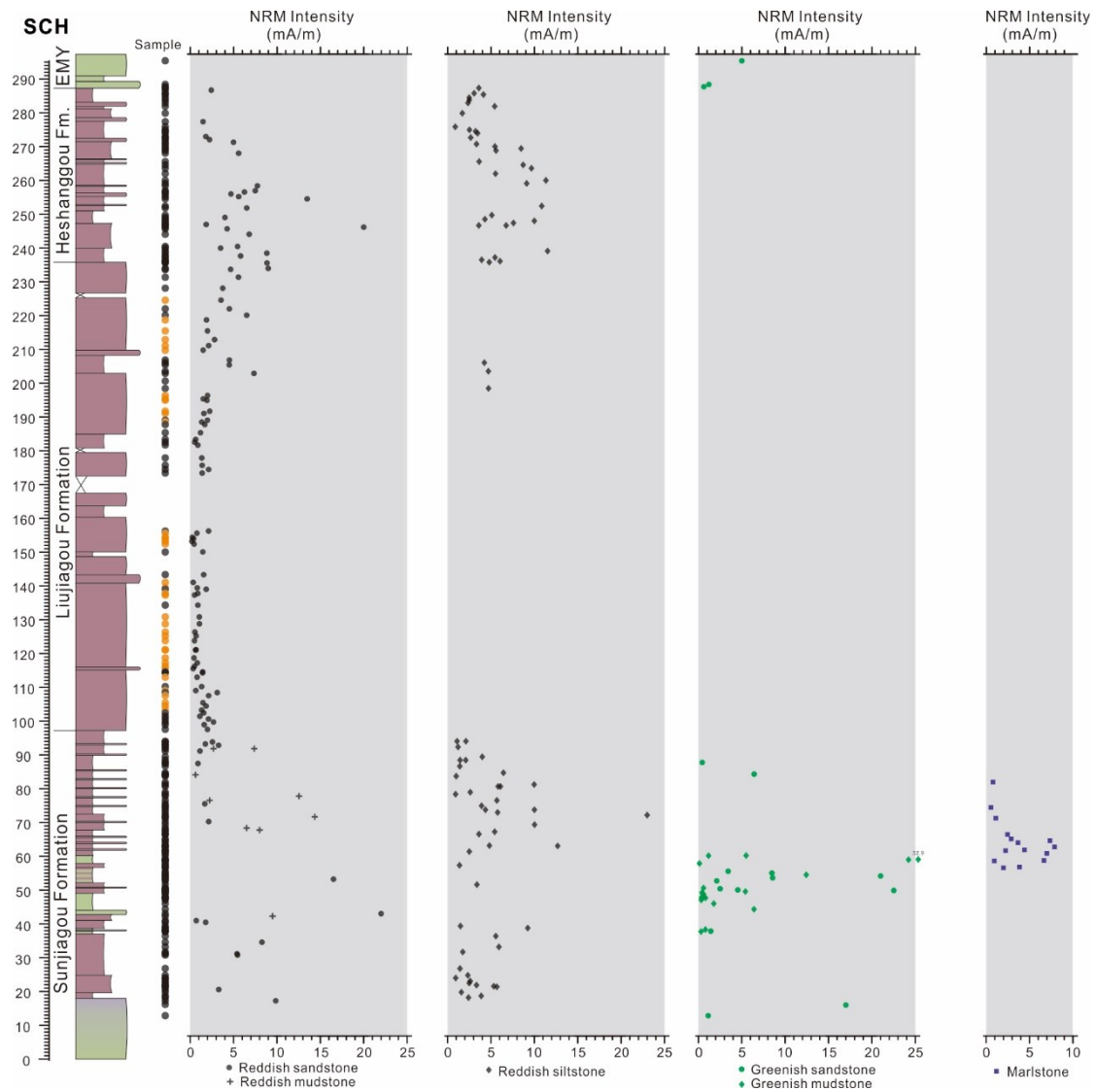
73 radioisotopically-dated ash bed indicated. B), Marine flooding influenced interval in the middle part  
74 of the Sunjiagou Formation, which is characterized by green mudstone where the mixed marine-  
75 terrestrial biota was found (Chu et al., 2019). The inferred PTB lies close to the top of the photograph.  
76 C), Alternating mudstone and sandstone just above the PTB, as showed in inset in B. (D),  
77 Multistorey sandstones in the lower portion of the Liujiagou Formation. E), The lowermost massive  
78 fine-grained sandstone displays a low-relief erosional contact (at sharp contact) with the underlying  
79 mud-rich (coastal environment) of the upper Sunjiagou Formation. F), Mud clasts of a varied size  
80 are common and weathered out leaving the holes. G), The laterally extensive sand-bodies are  
81 stacked lenticular channellised sandstones. The hammer is 25 cm in length. H), Thick sandstone of  
82 the uppermost Liujiagou Formation fining-upwards to the overlying red siltstone-dominated  
83 Heshanggou Formation, with a conformable contact. I), Green massive sandstones of the basal  
84 Ermaying Formation overlying the Heshanggou Formation, with a clear erosional contact (dotted  
85 line).

86

## 87 **2. Magnetic information**

### 88 **2.1 NRM intensity**

89 At the Shichuanhe section several lithologies were encountered. Green sandstone present in the  
90 lowermost and topmost parts of the section. The Permian–Triassic Boundary interval is dominated  
91 by red siliciclastics, with green mudstone occurring in the middle part of the Sunjiagou Formation  
92 within the marine influenced interval. Marlstone intervals are scattered in the upper of the Sunjiagou  
93 Formation. Generally, reddish sediments have higher (untreated) natural remanent magnetization  
94 (NRM) intensities than the greenish lithologies (Fig. S3). Around half of the mudstones have rather  
95 lower NRM intensities  $< 1$  mA/m, although exceptions up to 30 mA/m occur. Generally red siltstone  
96 and mudstone have higher NRM intensity than reddish sandstone. The sandstone dominated  
97 Liujiagou Formation has the lowest NRM intensity with respect to the Sunjiagou and Heshanggou  
98 formations.



99

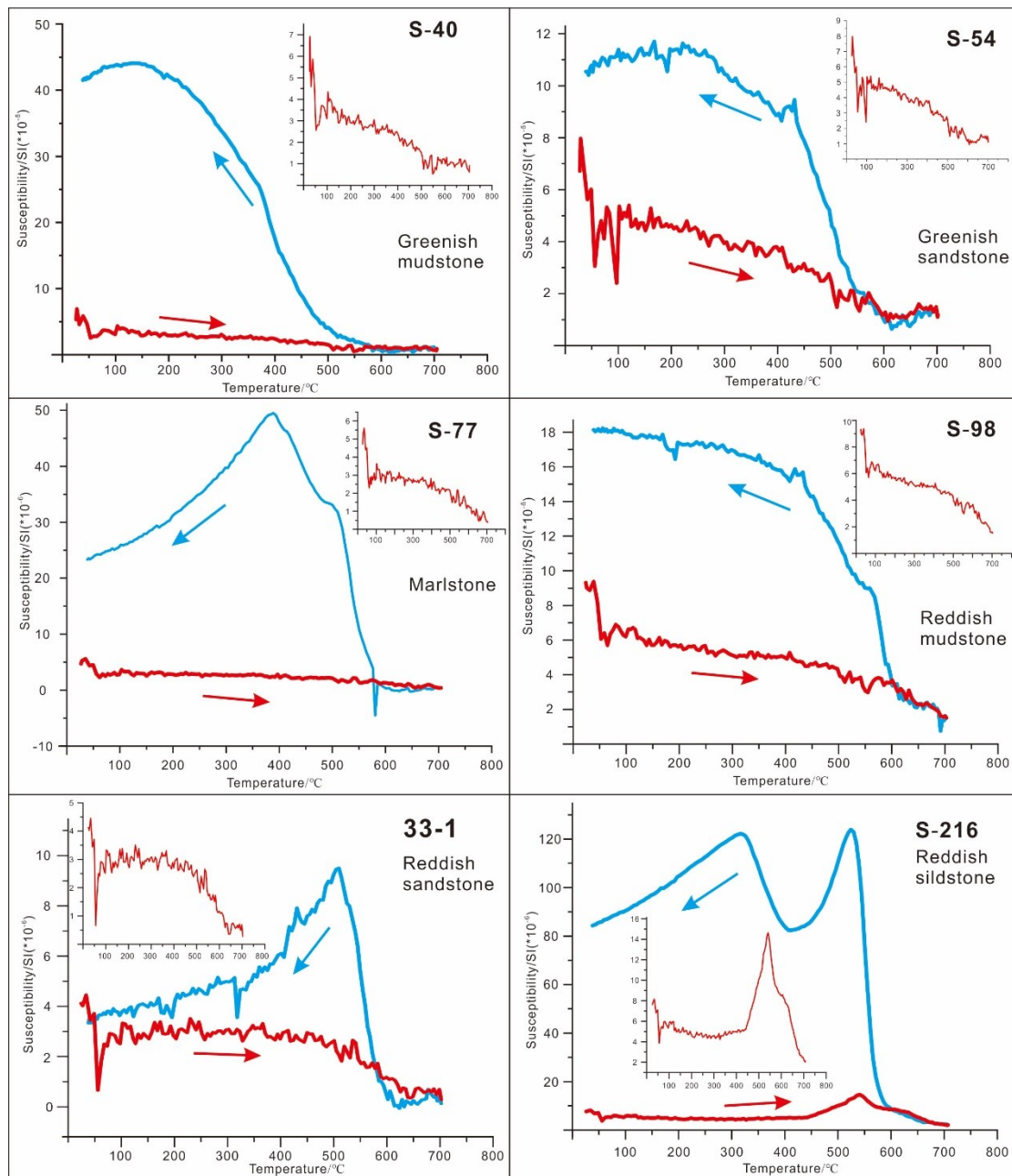
100 Figure S3. Variations of NRM intensity with lithology and body color. You need a mA/m scale on  
 101 all these plots

102

103 **2.2 Thermomagnetic curve**

104 The temperature dependence of magnetic susceptibility during heating and cooling cycles of  
 105 typical samples were measured in air (Fig. S4). All specimens display low initial susceptibility  
 106 which mostly decreases with increasing temperature. The heating and cooling curves are largely  
 107 irreversible, with cooling curves show conspicuously higher susceptibilities below 585°C, which  
 108 probably indicates newly formed magnetite due to clay and/or Fe-silicate decomposition during  
 109 heating (Deng et al., 2001; Jiang et al., 2015). For the green lithologies (specimens S-40 and S-54),  
 110 distinct drops in susceptibility are observed at 500-580°C, corresponding to the Curie temperature  
 111 of magnetite. The subsequent small rise of magnetic susceptibilities above 600°C could be

112 uncorrected drift or additional oxidation/alteration. For the red sediment samples the susceptibilities  
 113 consistently decrease to 700°C, indicative of hematite. Specimen S-216 shows a clear rise of  
 114 susceptibility from 450°C, which then decreases in the vicinity of 585°C and near 700°C, implying  
 115 the presence of both magnetite and hematite (although the magnetite may be alteration-generated  
 116 from heating starting at ca. 450°C). Goethite is probably also present according to the drop of  
 117 susceptibility upon heating below 100°C (De Boer and Dekkers, 1998). Thus, the main magnetic  
 118 carriers at SCH are mainly hematite, with magnetite more important in the greener lithologies.



119  
 120 Figure S4. K-T curves of representative specimens.

### 122 3. U-Pb geochronology methods and results

#### 123 Methods

124 Zircons were separated from a ~1 cm thick ash bed in the middle part of the Sunjiagou Formation  
125 at the SCH section (Fig. S1 and S2). After pulverization using a shatterbox, heavy minerals were  
126 separated using standard magnetic and high-density liquid separation techniques; several hundred  
127 zircon grains were obtained from the > 2,000 g sample. At least 200 zircon grains were selected,  
128 which were mounted in epoxy resin and polished down to expose their internal structures for  
129 subsequent cath-odoluminescence (CL) imaging.

130 The U-Pb isotopic and trace element analyses of zircons were conducted at the Mineral Rock  
131 Laboratory in Hubei Province, Geological Experimental Testing Center, using a Agilent 7700X  
132 inductively coupled plasma mass spectrometer (ICP-MS) coupled to a Geolas Pro laser ablation  
133 system. For detailed methods refer to [Liu et al. \(2008\)](#). Zircon was ablated with a laser beam of 32  
134  $\mu\text{m}$ -diameter. Offline data selection, integration of background and analyte signals, time-drift  
135 corrections, and quantitative calibrations of the raw U-Pb and trace element data were analyzed  
136 through ICPMSDataCal ([Liu et al., 2010](#)). Age interpretations are based on  $^{206}\text{Pb}/^{238}\text{U}$  dates. Errors  
137 are at  $1\sigma$  analytical uncertainty.

138 Eight prismatic and multifaceted zircon grains (some with axial glass inclusions) were selected  
139 under binocular microscope and were analyzed by the U-Pb CA-ID-TIMS method at the  
140 Massachusetts Institute of Technology (MIT) Isotope Laboratory, USA, following the general  
141 analytical procedures described in [Ramezani et al. \(2011\)](#). The selected zircons were pre-treated by  
142 a chemical abrasion technique modified after [Mattinson \(2005\)](#), which involved thermal annealing  
143 at  $900^\circ\text{C}$  for 60 hours and partial dissolution in 28M HF inside hydrothermal vessels at  $210^\circ\text{C}$  for  
144 12 hours, in order to mitigate the effects of radiation-induced Pb loss. Thoroughly fluxed and rinsed  
145 grain were then spiked with the EARTHTIME ET535 mixed  $^{205}\text{Pb}$ - $^{233}\text{U}$ - $^{235}\text{U}$  tracer ([Condon et al.,](#)  
146 [2015](#); [McLean et al., 2015](#)), before complete dissolution in HF for 48 hours followed by an anion-  
147 exchange column chemistry for purification of Pb and U. Measurement of the Pb and U isotopes  
148 were carried out on a VG Sector 54 multi-collector mass spectrometers equipped with Daly ion-  
149 counting systems at MIT.

150 Isotopic data reduction, date calculation and error propagation used the applications Tripoli  
151 and ET\_Redux and their algorithms ([Bowring et al., 2011](#); [McLean et al., 2011](#)). Complete U-Pb



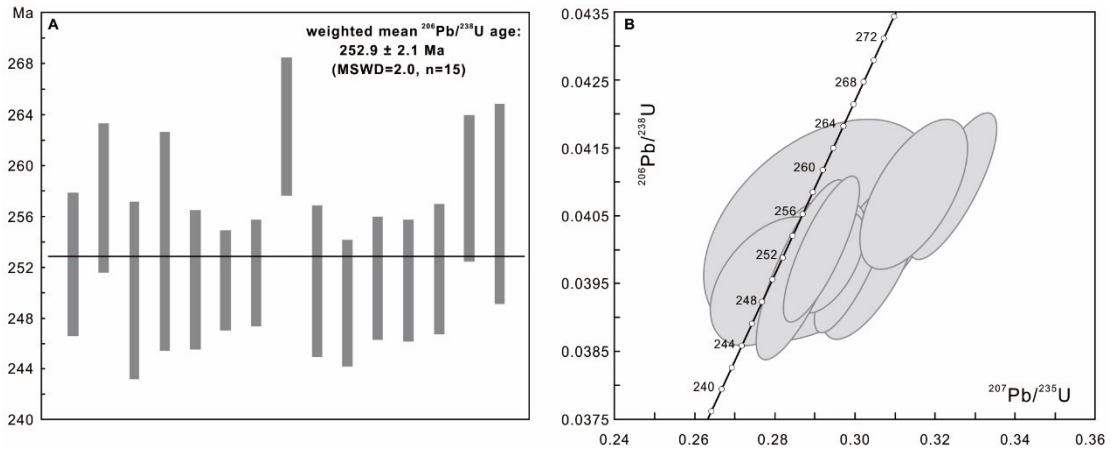
152 isotopic data are given in Supplementary Data C. All analyses were corrected for initial  $^{230}\text{Th}$   
153 disequilibrium using a value of 2.8 as the best estimate for the Th/U ratio of the parent magma. The  
154 ash bed age is calculated based on the weighted mean  $^{206}\text{Pb}/^{238}\text{U}$  date of zircons after excluding  
155 outlier analyses. The age uncertainty is reported at a 95% confidence interval and in the format  
156  $\pm x/y/z$  Ma, where x is the analytical (internal) uncertainty only, y includes the additional tracer  
157 calibration error and z includes the latter as well as the  $^{238}\text{U}$  decay constant error of [Jaffey et al.](#)  
158 [\(1971\)](#). In order to compare the calculated age with those from other ID-TIMS U-Pb laboratories  
159 not using the EARTHTIME tracer (or from other U-Pb techniques), the  $\pm y$  for either set of data must  
160 be taken into account.

## 161

## 162 **Results**

163 The LA-ICP-MS method is firstly employed to constrain the age distribution of the ash bed. Fifteen  
164 grains from forty analyzed zircons by LA-ICP-MS show ages ranging from  $263\pm 2.7$  Ma to  $249\pm 2.5$   
165 Ma (Fig. S5; Supplementary data C). Subsequently, eight zircons were analyzed by CA-ID-TIMS  
166 at MIT, which yielded a weighted mean age of  $252.25\pm 0.15$  Ma ( $n=4$ ), as well as four significantly  
167 younger Jurassic and Cretaceous ages (Supplementary data C). These data are rejected in this study  
168 because: 1) fresh ashes were sampled very carefully in the field, which were collected after digging  
169 and removing of superficial sediments; 2) the youngest strata exposed within the studied section is  
170 late Triassic, which means that those younger ages are unlikely to be contamination from younger  
171 detritus in the outcrops; 3) the LA-ICP-MS results provide maximum depositional ages with a wide  
172 range, no dates younger than  $\sim 240$  Ma are found. Therefore, the Jurassic and Cretaceous ages are  
173 in conflict with this evidence and were not used.

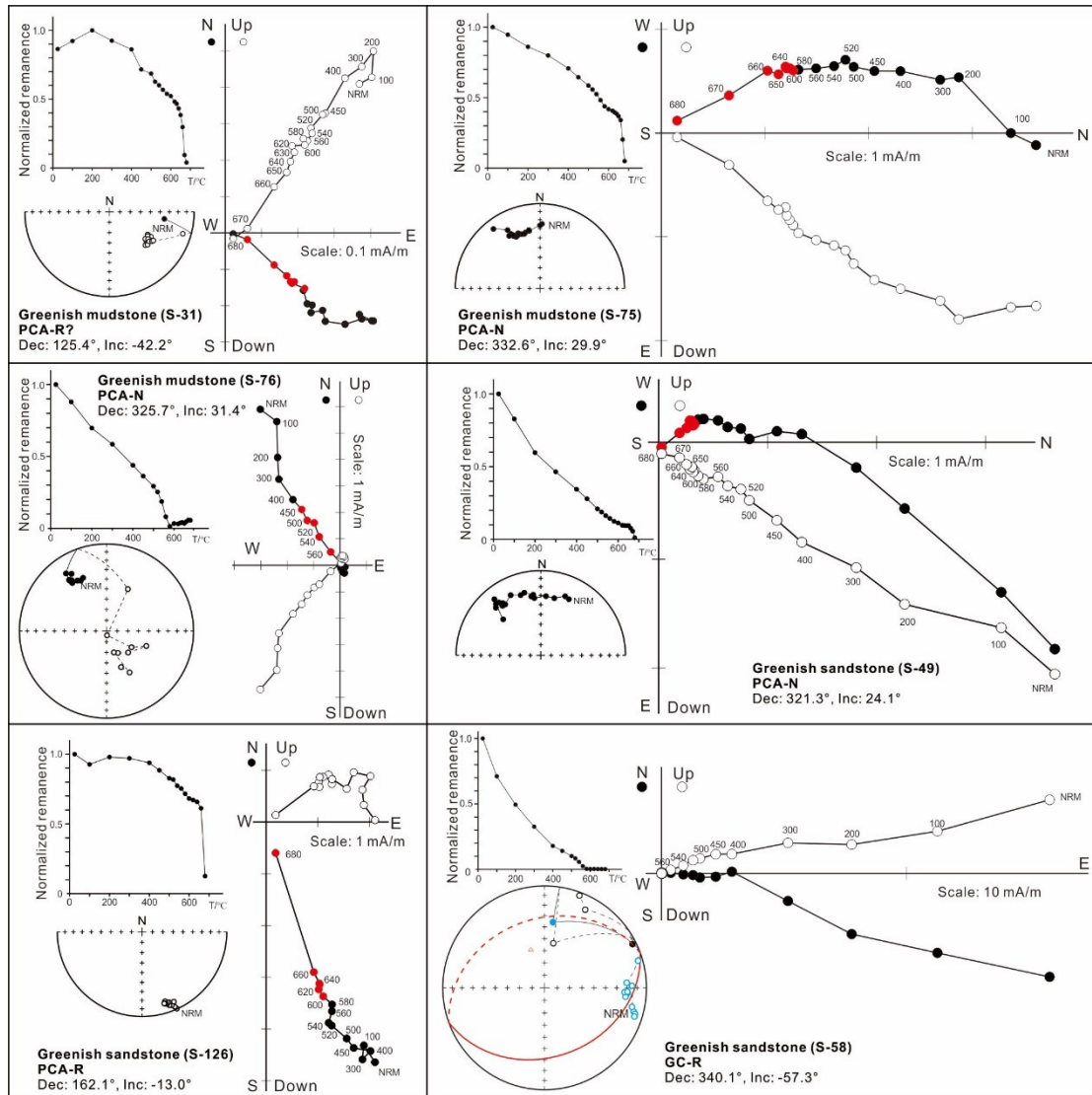
174



175

176 Figure S5. U-Pb dating results for zircons analyzed by LA-ICP-MS.

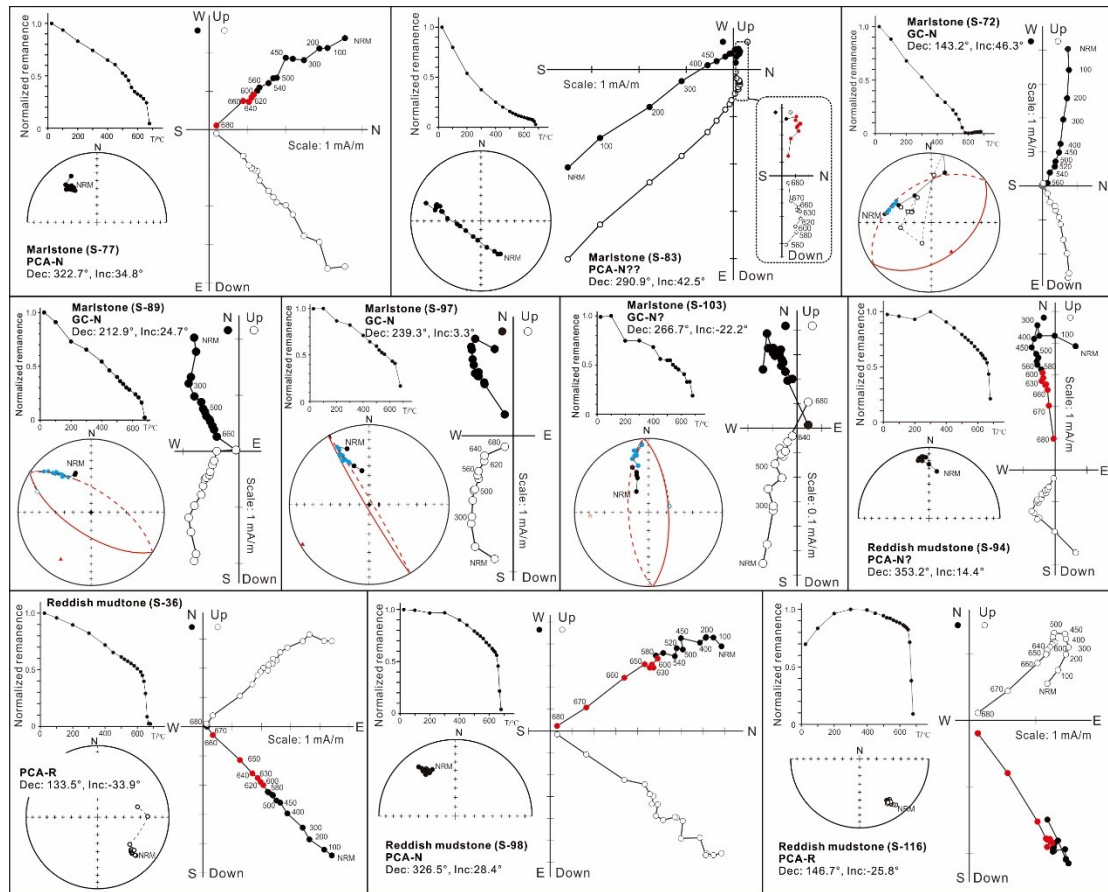
177



178

179 Fig S6. Demagnetization behaviors of greenish mudstone and sandstone specimens, Sunjiagou

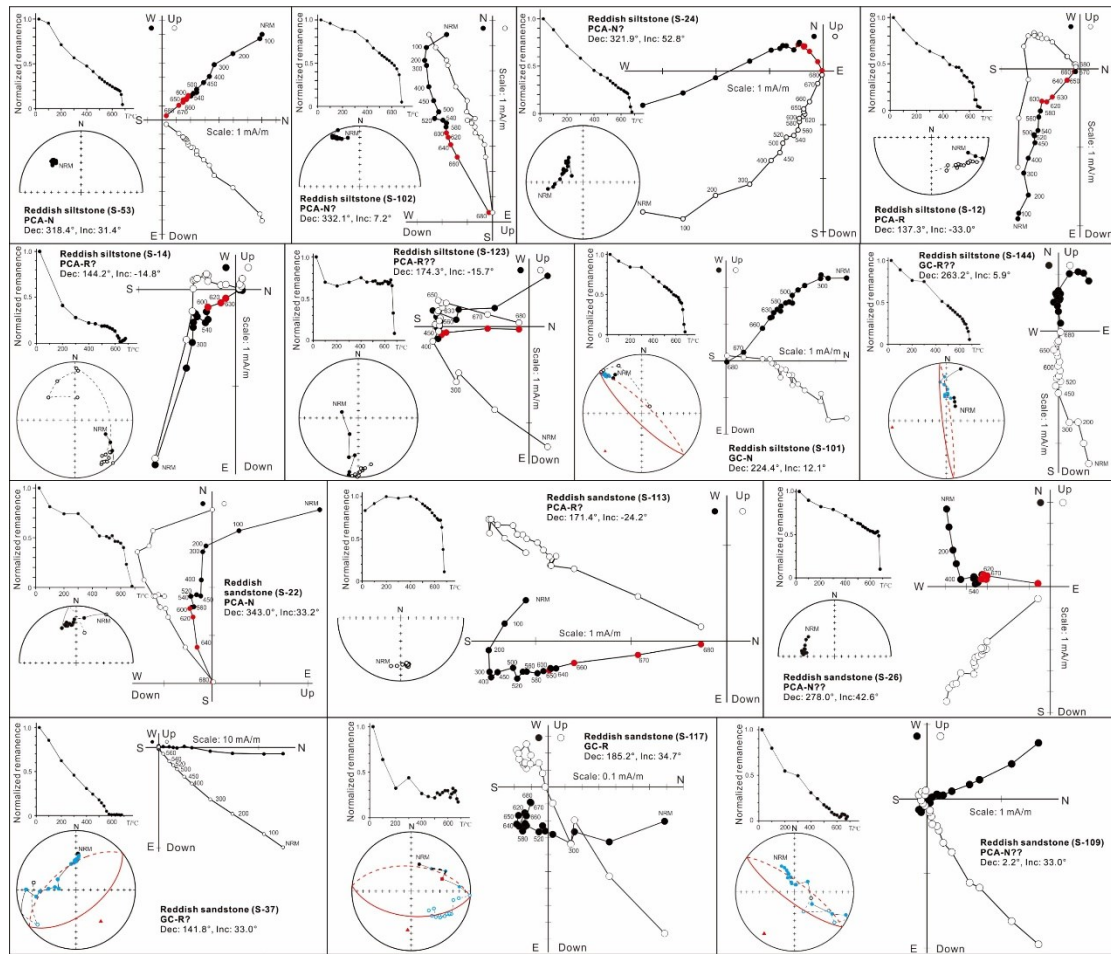
180 Formation.



181

182

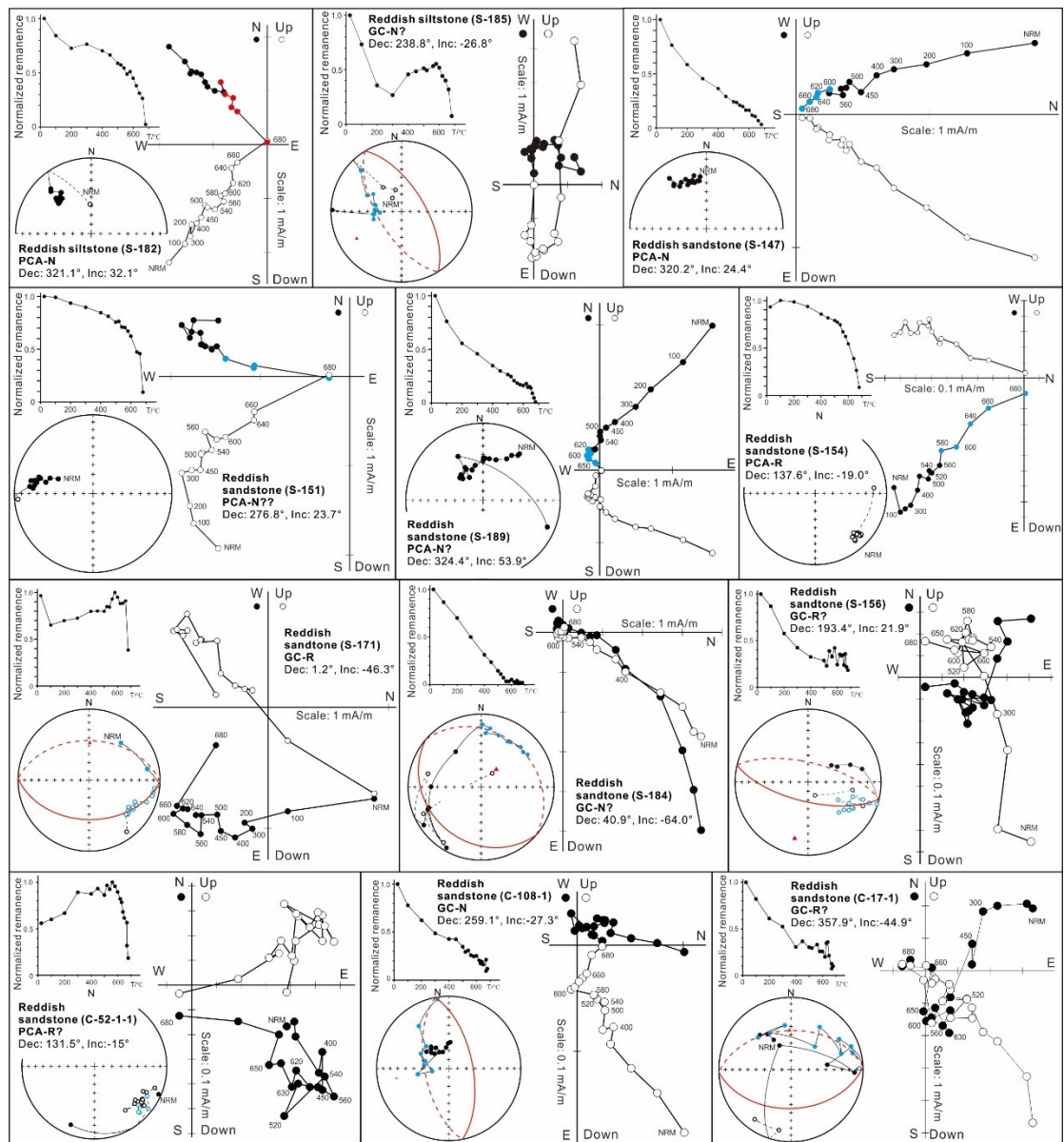
Fig S7. Demagnetization behavior of marlstone and red mudstone specimens, Sunjiagou Formation.



183

184

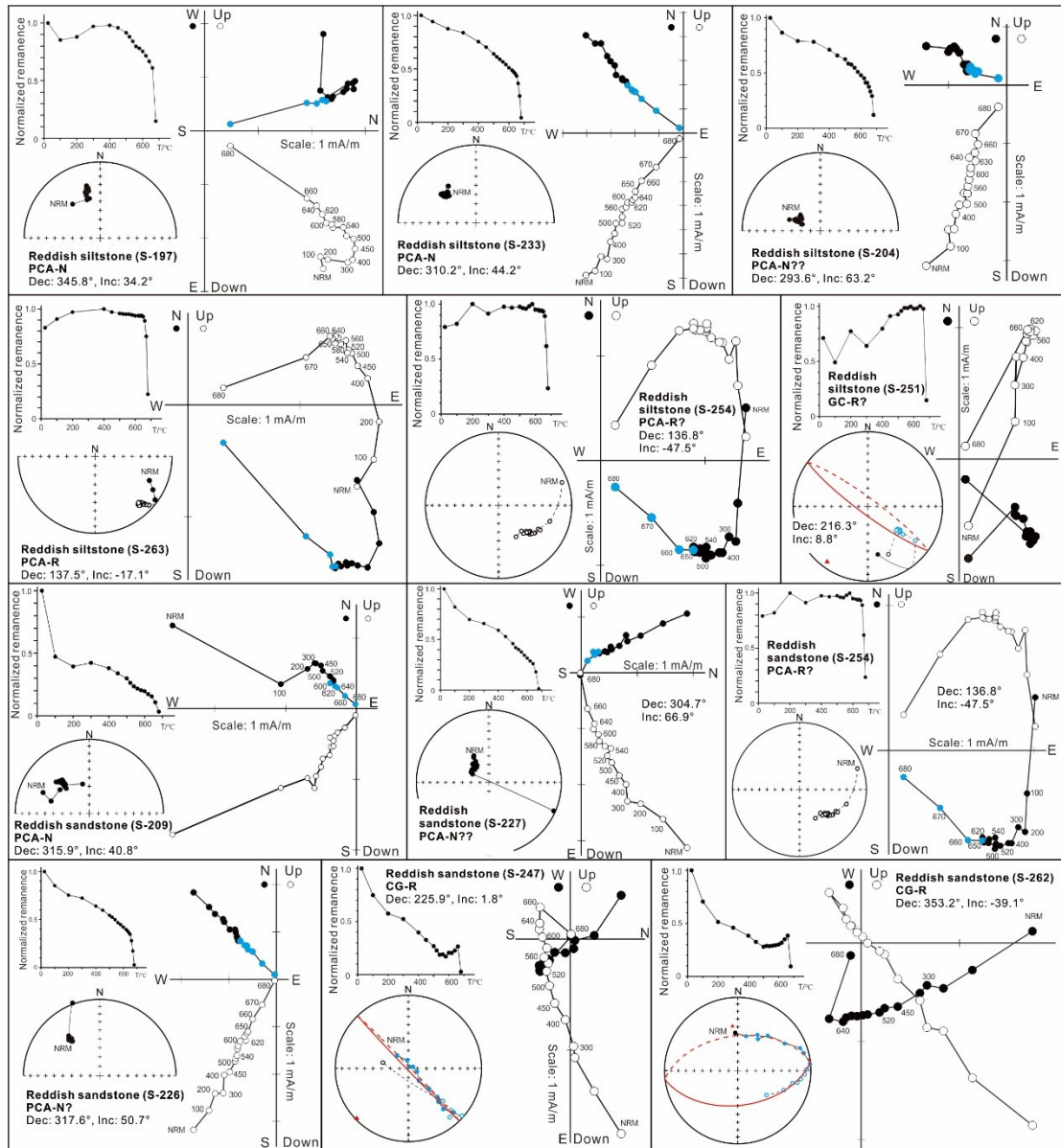
Fig S8. Demagnetization behavior of red siltstone and sandstone specimens, Sunjiagou Formation.



185

186

Fig S9. Demagnetization behaviors of red siltstone and sandstone specimens, Liujiagou Formation.



187

188 Fig S10. Demagnetization behavior of specimens with red-colored lithologies, Heshangou

189 Formation.

190

191

192

193

194

195

196

197

199 Table S1. Mean directions, reversal test and virtual geomagnetic poles (VGP) for samples with  
 200 different directional quality-ratings.  $D_s$ ,  $I_s$ ,  $K_s$  and  $\alpha_{95}$  are declination, inclination Fisher dispersion  
 201 and the 95% confidence cone in stratigraphic coordinates. (s/t) in polarity column are specimens in  
 202 the set and total in the set.  $G_o$ ,  $G_c$  are observed and critical angle for the McFadden & McEhinney  
 203 (1990) reversal test and the pass categories (Ra, Rb, Rc). Give site latitude and longitude here.

Mean direction (°) of different demagnetization behaviours											
SCH	Polarity	Mean site direction (°)				Reversal test ( $G_o/G_c$ )	Virtual Geomagnetic Pole (VGP) (°)				
		$D_s$	$I_s$	$K_s$	$\alpha_{95}$		Lat.	Long.	$\delta p/\delta m$	Paleolat.	
Line fits (142/256)	S1(77/142)	N(59/77)	326.3	32.4	39.96	3.0	Rb (5.86/6.05)*	55.0	356.1	1.62/2.90	16.7 N
		R(18/77)	147.1	-26.6	45.51	5.3					
	N+R		325.6	31.1	39.76	2.6	Rb (5.81/6.05)*				
	S2(47/142)	N(34/47)	322.8	36.9	17.14	6.1	Rc (6.2/11.43)*	54.3	2.8	3.41/5.9	19.4 N
		R(13/47)	145.4	-31.1	18.61	9.9					
	N+R		323.5	35.3	17.54	5.1	Rc (6.2/11.43)*				
S3(18/142)											
GC fit (95/256)	T1(30/95)	N(8)+R(22)	325.2	34.5	66.70	3.2	Rb (3.97/8.92)	55.3	0.5	2.14/3.72	18.9 N
		Combined S1+T1	326.2	32.2	22.4	2.1	Ra (0.56/4.68)*	55.2	357.4	1.31/2.33	17.4 N
	T2(43/95)	N(17)+R(26)	325.4	35.5	22.45	4.7	Rb (2.97/9.71)	55.9	1.3	3.15/5.44	19.6 N
		Combined S1+T1	324.7	35.1	10.0	3.4	Rb (3.6/7.97)*	55.2	1.5	2.28/3.95	19.3 N
T3(22/95)											

\* used a common K value

204

205

206

207

#### 208 4. References

209 Bowring, J.F., McLean, N.M., Bowring, S.A., 2011. Engineering cyber infrastructure for U-Pb  
 210 geochronology: Tripoli and U-Pb\_Redux. *Geochemistry, Geophysics, Geosystems* 12,  
 211 Q0AA19, doi:10.1029/2010GC003479.

212 Chu, D.L., Tong, J.N., Benton, M.J., Yu, J.X., Huang, Y.F., 2019. Mixed continental-marine biotas  
 213 following the Permian–Triassic mass extinction in South and North China. *Palaeogeography,*  
 214 *Palaeoclimatology, Palaeoecology* 519, 95-107. <https://doi.org/10.1016/j.palaeo.2017.10.028>.

215 Condon, D.J., Schoene, B., McLean, N.M., Bowring, S.A., Parrish, R.R., 2015. Metrology and  
 216 traceability of U–Pb isotope dilution geochronology (EARTHTIME Tracer Calibration Part I).  
 217 *Geochimica et Cosmochimica Acta* 164, 464–480. <https://doi.org/10.1016/j.gca.2015.05.026>.

218 De Boer, C.B., and Dekkers, M.J., 1998. Thermomagnetic behaviour of haematite and goethite as a  
 219 function of grain size in various non-saturating magnetic fields. *Geophysical Journal*  
 220 *International*, 133, 541–552. <https://doi.org/10.1046/j.1365-246X.1998.00522.x>.

221 Deng, C., Zhu, R., Jackson, M.J., Verosub, K.L., Singer, M.J., 2001. Variability of the  
 222 temperature-dependent susceptibility of the Holocene eolian deposits in the Chinese loess  
 223 plateau: a pedogenesis indicator. *Physics and Chemistry of the Earth, Part A: Solid Earth and*  
 224 *Geodesy*, 26: 873-878. [https://doi.org/10.1016/S1464-1895\(01\)00135-1](https://doi.org/10.1016/S1464-1895(01)00135-1).

225 Guo, W.W., Tong, J.N., Tian, L., Chu, D.L., Bottjer, D.J., Shu, W.C., Ji, K.X., 2019. Secular

226 variations of ichnofossils from the terrestrial Late Permian–Middle Triassic succession at the  
227 Shichuanhe section in Shaanxi Province, North China. *Global and Planetary Change* 181,  
228 102978. <https://doi.org/10.1016/j.gloplacha.2019.102978>.

229 Jaffey, A.H., Flynn, K.F., Glendenin, L.E., Bentley, W.C., Essling, A.M., 1971. Precision  
230 measurement of half-lives and specific activities of  $^{235}\text{U}$  and  $^{238}\text{U}$ . *Physical review C* 4, 1889–  
231 1906. DOI: <https://doi.org/10.1103/PhysRevC.4.1889>.

232 Jiang, Z., Liu, Q., Zhao, X., Jin, C., Liu, C. and Li, S., 2015. Thermal magnetic behaviour of Al-  
233 substituted haematite mixed with clay minerals and its geological significance. *Geophysical*  
234 *Journal International*, 200, 130–143. <https://doi.org/10.1093/gji/ggu377>.

235 Liu, Y.S., Hu, Z.C., Gao, S., Günther, D., Xu, J., Gao, C.G., Chen, H.H., 2008. In situ analysis of  
236 major and trace elements of anhydrous minerals by LA-ICP-MS without applying an internal  
237 standard. *Chemical Geology* 257, 34–43.

238 Liu, Y.S., Hu, Z.C., Zong, K.Q., Gao, C.G., Gao, S., Xu, J., Chen, H.H., 2010. Reappraisal and  
239 refinement of zircon U-Pb isotope and trace element analyses by LA-ICP-MS. *Chinese Science*  
240 *Bulletin* 55, 1535–1546.

241 Mattinson, J.M., 2005. Zircon U–Pb chemical abrasion (“CA-TIMS”) method: Combined annealing  
242 and multi-step partial dissolution analysis for improved precision and accuracy of zircon ages.  
243 *Chemical Geology* 220, 47–66. <https://doi.org/10.1016/j.chemgeo.2005.03.011>.

244 McFadden, P.L., McElhinny, M.W., 1990. Classification of the reversal test in paleomagnetism.  
245 *Geophysical Journal International* 103, 725–729.

246 McLean, N.M., Bowring, J.F., Bowring, S.A., 2011. An algorithm for U-Pb isotope dilution data  
247 reduction and uncertainty propagation. *Geochemistry, Geophysics, Geosystems* 12, Q0AA18,  
248 doi:10.1029/2010GC003478.

249 McLean, N.M., Condon, D.J., Schoene, B., Bowring, S.A., 2015. Evaluating uncertainties in the  
250 calibration of isotopic reference materials and multi-element isotopic tracers (EARTHTIME  
251 Tracer Calibration Part II). *Geochimica et Cosmochimica Acta* 164, 481–501.  
252 <https://doi.org/10.1016/j.gca.2015.02.040>.

253 Ramezani, J., Hoke, G.D., Fastovsky, D.E., Bowring, A.S., Therrien, F., Dworkin, S.I., Atchley, S.C.,  
254 Nordt, L.C., 2011. High-precision U-Pb zircon geochronology of the Late Triassic Chinle  
255 Formation, Petrified Forest National Park (Arizona, USA): Temporal constraints on the early  
256 evolution of dinosaurs. *GSA Bulletin* 123: 2142–2159. <https://doi.org/10.1130/B30433.1>.

257 Yu, Y.Y., Tian, L., Chu, D.L., Song, H.Y., Guo, W.W., Tong, J.N., 2022. Latest Permian–Early  
258 Triassic paleoclimatic reconstruction by sedimentary and isotopic analyses of paleosols from  
259 the Shichuanhe section in central North China Basin[J]. *Palaeogeography, Palaeoclimatology,*  
260 *Palaeoecology*, 110726.